UNIVERSITY OF CALIFORNIA
RIVERSIDE

Development of Functional Inks Based on Quasi-2D and Quasi-1D Materials for Application in Printed Electronics

A Dissertation submitted in partial satisfaction
of the requirements for the degree of

Doctor of Philosophy

in

Chemical and Environmental Engineering

by

Saba Seyed Mahmoud Baraghani

March 2022

Dissertation Committee:
Dr. Fariborz Kargar, Co-Chairperson
Dr. Alexander A. Balandin, Co-Chairperson
Dr. Aleksandr G. Khitun

The Dissertation of Saba Seyedmahmoudbaraghani is approved:

Committee Chairperson

University of California, Riverside

Acknowledgements

I would like to express my sincere appreciation to my PhD advisors, Prof. Fariborz Kargar, and Prof. Alexander A. Balandin for their supervision and great direction during the course of my work. Prof. Kargar is the most compassionate person I have ever seen. He has helped me with each and every step of the work. Even for the times I was falling short or disappointed, he would motivate me and encourage me to move on with the rest of the work. His enthusiasm and patience throughout the project not only inspire me but also, is something I can apply in other aspects of life. I will be forever thankful to him for this experience. Prof. Balandin has thought me to look at the problems from a different point of view and think out of the box. He has always been very supportive of different ideas I might have had. Undoubtedly, this work would not have been possible without his guidance and support. I would also like to thank Prof. Alexander Khitun for taking the time to serve on my committee.

I would like to express my gratitude to Dr. Amirmahdi Mohammadzadeh who has helped me with all the required trainings and cleanroom skills and patiently guided me through the obstacles of my work as a senior student in the lab and a dear friend. I would also like to thank Zahra Barani for helping me with my presentations, her advice on different topics, and always being there for me whenever I needed help.

I would like to express my gratitude to our collaborators from University of Nebraska, Dr. Alexander Sinitskii, Dr. Alexey Lipatov, and their PhD student Jehad Abourahma, and from University of Georgia, Professor Tina T. Salguero and her team for helping us with the synthesis of materials.

Many thanks to my friends and fellow lab mates in Nano Device Laboratory (NDL) and at Phonon Optimized Engineered Materials (POEM) Center, Subhajit Ghosh, Sriharsha Sudhindra, and Dylan Wright for helping me in different ways to improve my research level.

My deepest gratitude goes to my parents (Nasrin and Jalal) for all their sacrifices and all they have done for me to the point I am standing today and to my lovely sister (Saghi) who has been by my side with all her heart. I would also like to express my sincerest appreciation to Shahab, Ellie and Saba Bonakdar-Tehrani who have been like family to me from the day I stepped foot on the soil of US. I would like to specially thank my dearest friends Sanaz Gharachorloo and Siavash Ghalami Fard for their moral support throughout my work.

The text of this dissertation, in part or in full, is a reprint of the material as it appears in the following journals:

- Baraghani, S. *et al.* Printed Electronic Devices with Inks of TiS_3 Quasi-One-Dimensional van der Waals Material. *ACS Appl. Mater. Interfaces* **13**, 47033–47042 (2021).

Dedicated to

My parents

Nasrin and Jalal

My Sister

Saghi

And to my second family

Ellie, Shahab, Saba

ABSTRACT OF THE DISSERTATION

Development of Functional Inks Based on Quasi-2D and Quasi-1D Materials for Application in Printed Electronics

by

Saba Seyedmahmoudbaraghani

Doctor of Philosophy, Graduate Program in Chemical and Environmental Engineering
University of California, Riverside, March 2022
Dr. Fariborz Kargar, Co-Chairperson
Dr. Alexander A. Balandin, Co-Chairperson

Printed electronics technology, in which printing techniques are used with novel functional materials to manufacture electronic devices, has recently attracted a lot of attention. This is because utilization of printing process facilitates fabrication of higher volume of devices with lower cost and processing requirements compared to the conventional fabrication methods. Different functional materials have been used in the inks employed by various printing techniques. Recently, attention has been shifted towards a group of van der Waals materials with quasi-1D and quasi-2D structures such as transition metal chalcogenides. In this dissertation research, I report on the fabrication and characterization of electronic devices printed with inks of quasi-1D and quasi-2D van der

Waals materials. In the first part of the dissertation research, the ink was prepared by the liquid-phase exfoliation of crystals of TiS_3 semiconductor into quasi-1D nanoribbons dispersed in a mixture of ethanol and ethylene glycol. The ink was used to print electronic conducting channels. The temperature-dependent electrical measurements indicated that electron transport in the printed devices is dominated by the electron hopping mechanisms. The low-frequency electronic noise in the printed devices was of $1/f^{\gamma}$-type with $\gamma \sim 1$ near room temperature (f is the frequency). The abrupt changes in the temperature dependence of the noise spectral density and γ parameter can be indicative of the phase transition in individual TiS_3 nanoribbons as well as modifications in the hopping transport regime. In the second part of the dissertation research, I used quasi-2D 1T-TaS_2, which is a charge-density-wave material, for ink preparation. The two-terminal devices with 1T-TaS_2 channels were printed on Si/SiO_2 substrates. It has been demonstrated that the electrical conduction properties are preserved despite the use of solvents. The temperature-dependent electrical and low-frequency noise measurements indicated that the charge-density-wave phase transitions can be successfully induced in the printed devices. The results of this dissertation research are important for the development of printed electronics with innovative inks of quasi-1D and quasi-2D van der Waals materials.

Contents

List of Figures

List of Tables

1 Introduction and Overview

A set of electronic devices fabricated by utilizing printing techniques is called printed electronics. Printing can facilitate low-cost and high-volume production of electronics. Compared to the conventional device fabrication techniques that require many and costly steps, printing can drastically reduce the processing steps and the amount of labor.[1] In addition, it eliminates the need for device production on rigid substrates such as silicon and paves the way for the production of electronic devices on substrates such as PET and paper.[2–4] The latter is an important advantage in the field of flexible and wearable electronics and the internet of things (IoT).[1] Up to now, printed electronics have been used for many different applications such as solar cells,[5,6] capacitors,[7,8] sensors,[9,10] flexible displays,[11] field-effect transistors (FETs),[12,13] and smart packaging.[14]

Many different materials have been used as building blocks for functional inks in printing applications including metal nanoparticles,[15–18] graphene and carbon nanotubes,[19,20] and different oxide materials.[1] Among these materials, there have recently been numerous work on inks with quasi-2D transition metal dichalcogenide (TMD) van der Waals (vdW) materials.[21–25] The 1T polymorph of TaS_2, a layered transition metal dichalcogenide (TMD), is particularly interesting due to its charge-density-wave (CDW) transitions. This material has two transitions above room temperature making it a suitable candidate for many electronic and optoelectronic applications such as high-speed memory devices,[26] CDW oscillators,[27–29] and possible transistor-less logic circuits based on CDW.[30]

Transition metal chalcogenides (TMT) is another family of crystal structures that recently have received much attention owing to their quasi-1D structure. TMTs have shown extraordinary electrical properties such as high breakdown voltage, exceeding that of conventional metallic interconnects.[31] Field-effect transistors (FETs) based on few-layered TiS_3 have shown mobilities and ON/OFF ratios higher than or comparable to the well-known MoS_2-based FETs.[32–34] Up until now, despite many reports on printing electronics using layered materials, there are no studies on the synthesis and application of inks based on quasi-1D vdW and quasi-2D CDW materials. In this dissertation, the application of functional inks prepared by quasi-1D TiS_3 and quasi-2D CDW 1T-TaS_2 in two-terminal electronic printed devices are presented and their electronic transport and noise properties are measured and discussed. It is revealed that the electron transport mechanism in the printed TiS_3 devices is mainly dominated by the hopping mechanism. The low-frequency noise data elucidate a possible phase change or change of hopping transport regimes. The results of electronic transport measurements on devices with 1T-TaS_2 confirm the two CDW phase transitions in printed devices. These results are confirmed with low-frequency noise spectroscopy data.

1.1 Outline of the Dissertation

This dissertation includes the following chapters:

- Chapter 2: This chapter reviews different printing techniques and ink requirements.

- Chapter 3: This chapter explains the procedure of making the ink, printing, and device fabrication in detail. Images and schematics are provided to enable the reader to reproduce the whole process. The instrumentation to characterize the printed devices is also explained.
- Chapter 4: This chapter presents the demonstration of two-terminal devices based on quasi-1D TiS_3 nanoribbons. The details of tailoring the ink properties to ensure high printing quality is also explained.
- Chapter 5: In this chapter, the results of electronic and noise measurements of two-terminal devices based on quasi-2D CDW 1T-TaS_2 inks are presented.

2 Introduction to Printed Electronics

2.1 Printed Electronics

Solid-state-based devices have impacted human life substantially since their first introduction. These devices have gone through various development stages throughout the years. For example, the first generation of transistors utilized germanium, but soon germanium was switched to silicon because of its outstanding physical and electronic properties.[35] In spite of the advancements in the fabrication of electronic devices based on Si, still there are fundamental limitations especially when it comes to the large area, high volume production of devices, or the production of electronic devices that require more flexibility. Traditional methods to fabricate solid-state devices include the usage of extensive cleanroom settings and expensive instrumentation. In addition, utilization of high-temperature and low-pressure (for example during the chemical vapor deposition process), and harsh environments during the etching processes limits the usage of many substrates including flexible substrates.[1] For these reasons, there has been a search for alternative techniques, such as printing methods, that can replace the costly conventional fabrication methods. Compared to the traditional methods of electronics manufacturing, printing can drastically reduce the amount of energy and labor that leads to a reduction of costs. In addition to low cost, this method enables high volume fabrication of electronics even on flexible substrates.[1] However these advantages come with a downfall of lower

precision in printed electronic devices compared to devices made with cleanroom nanofabrication methods.

The utilization of printed electronics can facilitate the high-speed growth of the upcoming internet of things (IoT) and wearable electronics.[1] Thus, there has been a great interest in printed electronics for application in many different areas such as printed circuitry,[36] energy conversion and storage devices (*e.g.*, solar cells, capacitors, etc.),[37] sensors, field-effect transistors (FETs),[38] flexible displays,[39] and smart packaging.[40] There are different printing techniques that can be used for device manufacturing for any of these applications including drop-casting, screen printing, inkjet printing, Gravure printing, and flexographic printing.[1]

2.1.1 Drop Casting

Drop casting is an easy and tunable method of deposition of material on different substrates. In this method, drops of the solution are spread on the surface and are left to dry under controlled conditions. Morphology and thickness of the deposited sample can be controlled by the adjustment of different parameters. For example, variation of the environmental conditions such as temperature and pressure can lead to a change in the morphology of the dried trace. The thickness of the deposited material depends on the droplet volume and pigment concentration. Despite being simple and cost-effective, the drop-casting method can only be utilized for substrates with small surface areas which limits its use as a common method in the fabrication of printed and flexible electronics.[41]

2.1.2 Screen Printing

Screen printing is another inexpensive and straightforward method of printing on various substrates regardless of their rigidity. The process of printing consists of pushing the ink paste through a porous stencil to deposit the pattern onto the surface. Herein, there are four constituents to the process: the ink paste (an ink with very high viscosity), the screen, the substrate, and the squeegee.[42] Although this method proves to be very useful in the conventional printing industry, its resolution is rather low. It also requires extensive use of lithography for the fabrication of the screen.[42]

2.1.3 Inkjet Printing

Inkjet printing is a non-contact and mask-less printing technique in which ink droplets are jetted and deposited onto the substrate to generate the desired pattern designed electronically via a computer. There are two common jetting mechanisms: continuous inkjet and drop-on-demand (DoD). In the continuous process, the ink droplets are generated continuously to be deposited on the substrate whereas, in the DoD process, ink droplets are only generated if required. This can be done through the piezoelectric or thermal jetting mechanism.[1,43] In the piezoelectric mechanism, the ink is pushed out of the reservoir due to a pressure pulse caused by the piezoelectric material in the printhead. In the thermal mechanism, ink droplets are propelled as a result of bubbles generated after a

rapid heat-up of the ink. The DoD process is more commonly used for inkjet printing owing to its simpler operation compared to the continuous inkjet process.[44]

2.1.4 Gravure and Flexographic Printing

Flexography and gravure printing are printing techniques referred to as the continuous roll-to-roll (R2R) techniques. These methods are fast transfer and large area printing processes which are mainly used for industrial purposes such as packaging and books and newspapers printing. One of the main differences of the flexography and gravure printing processes is in the amount of applied pressure. Other differences include the ink transfer pathway and printing speed. The details of the printing procedures can be found in the literature.[45,46]

2.2 Comparison of Different Printing Methods

As indicated in the previous sections, printing techniques are different in various aspects. Therefore, one can select a printing process based on the application needs such as the desired printed feature size, production speed, and the type of substrate the print will be made on. A summary of some of the important parameters in the selection of the printing techniques is listed in Table 2.1. Based on the table, one can conclude that inkjet printing is a good choice for prototyping and lab-scale work due to its high precision and acceptable throughput.

Table 2.1. Comparison of different printing processes

Printing Method	Throughput	Precision	Required Ink
Drop Casting	Low	-	Low
Inkjet	Medium	High	Low
Screen	Medium	Low	Low
Gravure	Medium	Low	High
Flexographic	High	Low	High

2.3 Important Ink Parameters in Inkjet Printing

Various parameters affect the quality of inkjet printing. These factors include ink composition, its physical properties (*e.g.*, viscosity, surface tension, density, etc.), drying and spreading of the ink, and the required post-processing steps. The latter should be carried out to improve the physical and electrical properties of the printed device.

2.3.1 Ink Composition

First-ever inks were made in ancient China by mixing soot and gum resins to make an ink paste. Since then, so many developments have been made to the inks along with the evolution of the printing processes. This includes switching pigments from soot to colored plants and then to organic or inorganic chemicals. Additives were also mixed into the inks to make them suitable for modern printing processes. Nowadays, inks are generally composed of four major parts: pigments, binders, additives, and solvents.[47]

For graphical inks, pigments are used for ink coloration. There are also other pigments incorporated into the ink for some special functions. For instance, calcium

carbonate ($CaCO_3$) and titanium dioxide (TiO_2) are used for color intensity reduction and opaque ink production, respectively. Various other pigments can also be added to the ink for serving different functions such as gloss or protection against environmental conditions such as heat or humidity.[43]

With the advent of printed electronics, functional materials such as conductors, semiconductors, and dielectrics were imbodied in the inks as pigments.[48] Some of the functional materials that have been used in inks include metallic nanoparticles such as silver and copper,[16,49] organic materials such as Baytron-P, poly (4-vinyl phenol) (PVP), and polythiophene,[3] and carbon materials such as carbon black, graphene, and CNTs.[50,51] Recently, there has been an increasing interest in the utilization of layered 2-D materials as functional pigments owing to their unique material properties.[44]

Binders are usually polymers used to bind the pigment particles to each other and to the printing substrate. Ink binders may dry as a result of solvent evaporation. Otherwise, post-processing such as annealing or ultraviolet light exposure may be required to cure and harden the ink.[52] Binder selection for a specific ink is based on the physical properties required such as adhesion or gloss level. For example, cellulose is utilized as a binder to make the ink moisture resistant.[43]

Additives constitute a very small proportion of the inks with the purpose of modification or tailoring specific ink properties. Surfactants are an example of ink additives that are used to improve the wetting properties of the ink. The solvent, as suggested by its name, is a component to dilute other ink components and keep the ink in liquid form. Water or any type of organic solvent can be used in the ink. Depending on the printing method,

type of substrate, printing purpose, and drying conditions one can select the desired solvent. For instance, in high-speed printing processes such as gravure printing, solvents with higher drying rates should be chosen, whereas for screen printing, the solvent with a slower drying rate should be selected to avoid clogging up the mesh pores.[53]

2.3.2 Drying and Spreading of the Ink

Spreading and drying of the ink are the two crucial factors in the determination of the final print pattern morphology. The spreading of the ink during the printing process is defined by its wettability. The contact angle between the droplet and the underlying substrate, θ, is a measure of how well the ink spreads on the substrate (Figure 2.1). Contact angles larger than 90^o are indicative of poor wetting whereas angels smaller than 90^o suggest good wetting of the surface. In the printing process, the term 'good wetting' refers to a scenario when the ink is capable of spreading and maintaining contact with the substrate leading to a continuous trace. For this to happen, the solid interfacial surface tension should be greater than that of the ink. Therefore, it is easier to wet surfaces with higher surface energies like copper than the substrates with lower surface energies such as polytetrafluoroethylene (PTFE). As a rule of thumb, if the difference between the surface tension of the substrate and the ink falls in the range of ~7 to ~10 mN m^{-1}, a good wetting will be achieved. The contact angle is determined by Young's equation.[54] According to this equation, for a droplet, surrounded by gas or its vapor, on a homogeneous, smooth, ideal

surface, the relationship between the interfacial surface tensions of gas, solid, and liquid is given by:

$$\zeta_{sv} = \zeta_{sl} + \zeta_{lv}.\cos\theta, \tag{2.1}$$

where ζ_{sv}, ζ_{lv}, and ζ_{sl} are the surface tensions of the solid surface, liquid surface, and the solid-liquid interface, respectively.

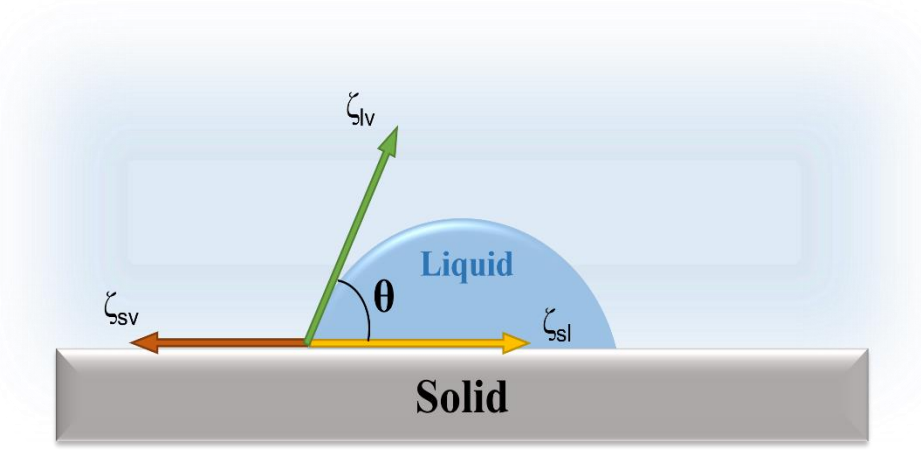

Figure 2.1. Schematic of a droplet on a solid surface.

Other than spreading, the ink drying rate plays an important role in the final morphology of the printed pattern and depends on the ink viscosity. For the inks with high viscosities such as the inks used for screen printing, rectangular cross-sectional profiles of the prints are indicative of a uniform deposition, drying, and distribution of the ink.[43] As the viscosity is lowered to more moderate ranges, the cross-sectional profile turns into

semi-circle geometries. It is worth noting that if the viscosity of the ink is too low, the cross-sectional profile will exhibit the so-called “coffee-ring” patterns which result in an undesired morphology.[43] Basically, this phenomenon happens because of non-uniform evaporation of the solvent during the ink droplet drying on the surface. When the ink droplet is dispensed onto the substrate, the contact line at the edge of the droplet-substrate interface has the highest surface area to volume ratio. This leads to faster evaporation rate of the solvent compared to the center of the droplet. The difference in the evaporation rate causes a concentration gradient across the droplet (lower solvent concentration at the edges). As a result, there is an outward convection flow carrying the pigments to the edges leaving little to no material at the center.[55] In addition to viscosity, drying, and environmental conditions have substantial impacts on this process.[56]

2.3.3 Ink Jetting Behavior

In the printing process, one has to make sure there is stable disposal of the ink droplets from the nozzle. This means droplets of the ink should form continuously without the formation of secondary (satellite) droplets[57] to eliminate ink deposition in unwanted areas. This behavior in the ink can be determined by paying close attention to the ink thermophysical properties determined by the dimensionless Z-number which is the inverse of the Ohnesorge number (Oh):

$$Z = \frac{1}{Oh} = \frac{\sqrt{\zeta \rho a}}{\eta}, \quad (2.2)$$

Here, a is the diameter of the nozzle, η is the viscosity of the ink, and ρ and ζ are the density and surface tension of the ink, respectively. Generally, it is considered that the optimum value of Z should lie between 1 to 14. If the Z value is higher than 14, there is a high possibility of satellite droplet formation. Z values less than 1 leads to the formation of elongated droplets or no ink droplet formation at all.[50,58,59]

2.3.4 Ink Preparation and Strategies to Improve Print Quality

Liquid phase exfoliation (LPE) is the conventional method for the preparation of functional inks with layered vdW materials. As the first step, materials are exfoliated in a liquid-phase environment such as n-methyl-2-pyrrolidone (NMP). The as-exfoliated dispersions are often used as inks for printing. However, the problem with this method of ink preparation is that the solvents used for exfoliation usually have a high boiling point. Thus, in this case, printing will be time-consuming since the solvent should evaporate at the end of the printing. In addition, high surface tension and low viscosity of these solvents prevent print lines with high quality. To address this issue, different approaches can be applied. One approach is to treat the surface to adjust the surface tension between the ink droplet and the substrate.[50] Another method is to use polymeric binders in the formulation of the ink. In this method, the exfoliated material by the LPE technique is first removed

from the initial solvent. The flakes are then dispersed again in another selected solvent mixed with a polymeric binder. Adding binders can adjust the viscosity of the ink. In addition, there is a chance for increasing the concentration of functional material in the ink using this method. However, it should be noted that the addition of binders in the ink can decrease the desired properties of the functional ink, such as its electrical conductivity. To account for this, post-processing and thermal annealing is necessary which makes the printing process more complicated. An alternative and simpler approach is to mix two different solvents. This will cause a uniform dispersion and drying of the ink as a result of the Marangoni effect during ink drying. The Marangoni effect happens due to the surface tension gradient caused by the difference in the temperature or composition. [60]

3 Fabrication of Printed Devices

3.1 Preparation of the Ink Using Liquid Phase Exfoliation

The conventional methods of device fabrication based on 1D or 2D materials include mechanical exfoliation of the material using a Scotch tape method.[29,61–64] Utilization of this method leads to nanomaterials with variable thickness and hinders the scale-up of the production of electronic devices.[65–67] Another method, is to synthesize the highly crystalline material using chemical vapor deposition (CVD) which is expensive and energy-intensive and requires a harsh environment (high temperature and vacuum).[68] Alternatively, solution-based synthesis has been employed as a simple, low-cost method that can be used for the preparation of functional inks. However, smaller flake size, thickness variation, and high defect density of the nanomaterials are inevitable while using this method.[69] Generally, two different approaches are taken for the solution-based synthesis of nanomaterial: top-down and bottom-up. Liquid phase exfoliation is a top-down method that is widely used for the preparation of functional inks owing to its simplicity and effectiveness. In this method, bulk crystals of the material are placed in a solvent and the weak van der Waals forces between the layers of the material are broken down using strong sonication or shear energy. Different solvents such as dimethylformamide (DMF), N-methyl-2-pyrrolidone (NMP), acetone, and ethanol have been used for exfoliation of 1D and 2D materials.[69–73] In this method, it is important to choose adequate solvents that match the surface energy of the layered material.

After the exfoliation, there might be a need to transfer the nanomaterial to a different solvent such as isopropyl alcohol (IPA). To do this, the as-exfoliated material is centrifuged at a high speed and then, the original solvent is collected from the top part. Afterward, the secondary solvent, the one that is actually used in the ink formulation, is added to the flakes. The mixture is sonicated for 15 minutes to ensure homogeneous dispersion of nanomaterial in the solvent. This process is repeated several times to make sure that the original solvent is fully removed.

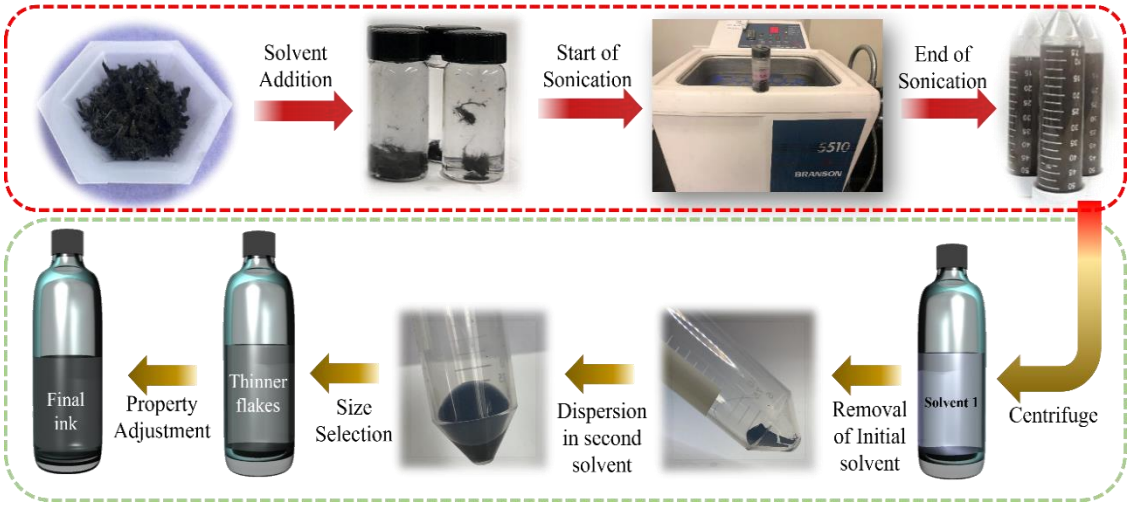

Figure 3.1. Schematic of the exfoliation and ink preparation steps. The red box represents the exfoliation process and the green box represent the solvent exchange, size selection, and adjustment of ink properties. Not all the steps in this box are necessary. For example, the solvent exchange and size selection steps can be skipped for some inks.

In the next step, the physical properties of the ink should be adjusted to obtain a Z-number between 1 to 14, as discussed in the previous sections. Figure 3.1 exhibits the whole process of ink preparation. In this study, ethylene glycol is used as a secondary solvent because of its high viscosity compared to the main solvent (usually ethanol or IPA)

to adjust the ink viscosity. Other than viscosity adjustment, the addition of ethylene glycol will suppress the formation of the coffee ring by causing the Marangoni effect in the ink droplet.[60]

3.2 Preparation of Device Contacts Using Electron-Beam Lithography

In this work, electron-beam lithography (EBL) is used to fabricate the gold contacts of printed devices. EBL is associated with multiple steps. For the scope of this work, the steps are as follows: (1) PMMA spin coating of the substrate, (2) writing the electrode pattern using EBL and development of the substrate, and (3) metallization and lift-off.

3.2.1 PMMA Spin Coating

Before writing the electrode pattern on the silicon substrate using EBL, the surface of the silicon should be covered with a thin layer of polymeric material resistant to electron beam such as polymethyl methacrylate (PMMA). The diced silicon wafers should be cleaned in advance for the PMMA spin coating. The cleaning process consists of sonicating the wafers in acetone followed by ethanol sonication for 5 minutes. The substrate is then dried with high purity nitrogen gas. Spin coating is used as the next step and for the deposition of PMMA on the substrates. To start the spin coating process, a few drops of PMMA is dropped on the wafer that has been previously placed on top of a holder disk in

the spin coater machine. Special care should be taken to avoid the formation of any air bubbles during this step. The spin coater is programmed with a special recipe for this process. This recipe consists of three steps: spreading, spinning, and stopping. The parameters are listed in Table 3.1.

Table 3.1. Different steps of the spin-coating recipe with conditions for proper coverage of the sample

	Speed (rpm)	**Duration (s)**	**Ramp Rate (rpm/s)**
Step 1 (spread)	400	3	400
Step 2 (spin)	4000	45	2000
Step 3 (stop)	0	2	2000

Note that faster spinning speeds usually lead to a thinner layer of PMMA on top of the silicon wafer. It is important to have the thickness of the resist smaller than the total thickness of the metal electrodes. Otherwise, the lift-off of the metals from the surface will be impossible. The recipe presented in Table 3.1 leads to a resist thickness of about 170 nm. After the spin coating is done, it is necessary to do post-treatment by heating up the resist to its glass transition temperature (T_g). For the 495 PMMA, T_g is between 100 ℃ and 160 ℃. So, the sample was kept at 185 ℃ for two minutes after each layer of resist is applied to the surface.

3.2.2 Writing and Development of Electrode Pattern

Electron beam lithography, which is a process of using electron beams to write patterns on an electron beam resist, is used for this step. This method is preferable compared to the conventional photolithographic methods because the shorter wavelength of electrons makes the writing of finer patterns with higher resolutions. In this equipment, the electron beam is steered by the magnetic deflectors based on the computer-assisted design (CAD) pattern. To follow the CAD pattern, the stage is moved by the stage controller and stage monitor. For this study, a Leo SUPRA 55 equipped with an electron-beam patterning system is utilized.[74,75] The electrodes were designed using DesignCAD software.

While using the EBL, one should know where the electrode patterns are going to be written. For this reason, a small dot of diluted silver paint is placed on the substrate surface prior to placing the sample in the chamber. Afterward, utilizing the scanning electron microscope at low voltage (around 5 kV), the shiny silver dot will be located on the substrate surface to determine where the electrode pattern should be written. To write the electrode pattern, the NPGS software and the pattern run file are used.

To complete the EBL process, the PMMA resist should be developed in a developer solution consisting of a mixture of methyl isobutyl ketone (MIBK) and isopropyl alcohol (IPA). The ratio of MIBK:IPA is 3:1 in the developer solution. This is to remove the parts exposed to the electron beam and make the sample ready for the metallization step. In order to do this, the sample is submerged in the developer solution for 20 s. It is then removed

from the solution and soaked in IPA for another 20 s. It is then dried using high-purity nitrogen gas. The quality of the written and developed pattern can be confirmed using an optical microscope.

3.2.3 Metallization and Lift-Off

To deposit the metal electrodes on the substrate, two different metals were used. Titanium and gold with the thickness ratio of 1 to 10 (5 nm Ti and 50 nm Au or 20 nm Ti and 200 nm Au) are deposited on the substrate at this step with titanium being the first layer. The reason for this structure is that titanium has good adhesion to the silicon wafer surface and can assist in better attachment of gold to the substrate. In this step, an electron beam evaporator is used for metal deposition. The samples are placed inside the chamber of the evaporator. The chamber is then pumped down to the pressure of 2×10^{-6} torr which is ideal for metal deposition. To deposit the titanium layer, a slow deposition rate of 0.5 Å/s is used. Subsequently, the deposition of the gold layer should be carried out with the same slow rate of 0.5 Å/s for the deposition of the first 10 nm of the layer, and then it is ramped up to 2 Å/s. After the deposition is done, the chamber should be left to cool down in vacuum before the samples can be removed. For this study, a Temescal Model BJD – 1800 electron beam evaporator is used. A schematic of this procedure is presented in Figure 3.2.

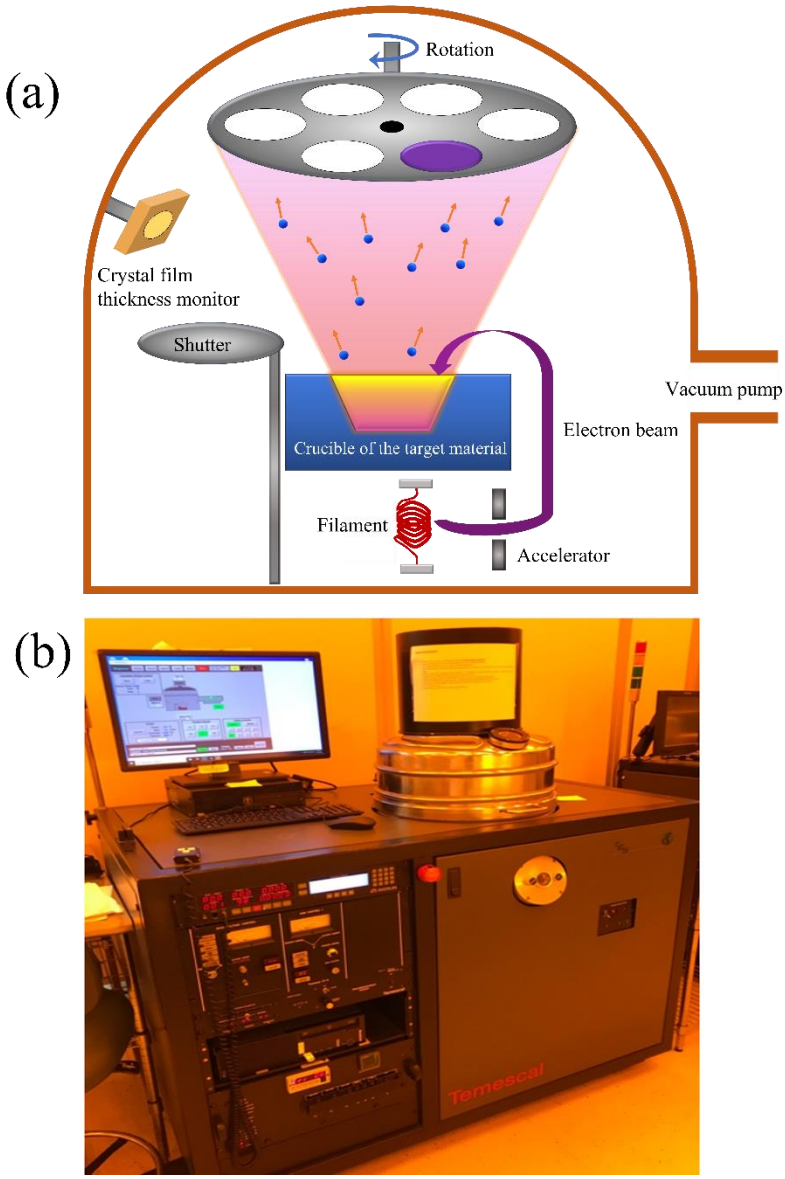

Figure 3.2. (a) schematic of an electron beam evaporator and its operating procedure, (b) actual image of an e-beam evaporator located at UCR's nanofabrication facility.

Following the metal deposition, the metalized part of the sample without any pattern should be removed in a lift-off step using acetone. If the thickness difference between the PMMA and the deposited metal is sufficiently large (as discussed in the previous sections),

by soaking the sample in acetone, all the excessive metal will lift off from the surface. One must make sure that all the excess metal is removed. Otherwise, the removal of the unwanted metallic parts would be impossible after the sample is taken out of acetone. The final pattern can then be checked using an optical microscope.

3.3 Printing of Functional Ink

After deposition of the contacts, the functional ink is printed on top of them using an inkjet printer. The printer used in this work is a Hyrel 30M material printer. To make the printing process similar to inkjet printing, the extruder head of the printer was swapped with a syringe head holder to make the printing of the inks possible. The silicon wafer with the gold electrodes is placed on top of the printed stage. The stage and printer head can move in different directions to follow the computer-assisted design (CAD) pattern for the print. The stage is also heated up to 60 ℃ to speed up the ink drying process and enhance the Marangoni flow inside the ink droplet leading to no coffee-ring formation.

Before printing, the ink was loaded in a syringe. To ensure fine print traces, a syringe needle with an appropriate diameter should be selected. As opposed to regular inkjet printers, the printer used in this work works based on the application of a small force on the syringe shaft to dispense the liquid. Having a syringe needle with a very small diameter will require more pressure on the shaft and makes the control of the ink droplet size harder. This will lead to poor condition in the final print. In this work, a gauge 27 blunt-end needle with an inner diameter of 210 μm was employed.

After the ink is loaded into the printer, the printing parameters should be adjusted. These parameters include the moving speed of the stage and the printer head, stage temperature, droplet volume, and the number of printing passes. All these parameters can be tuned using a built-in software called Repetrel. After each round of printing, the printed trace is left to dry before printing another layer on top. This step is repeated until the approximate desired thickness is achieved. After the printing is finished, the pattern is checked with an optical microscope to ensure the quality of the print. An image of the printer used for this work is presented in Figure 3.3.

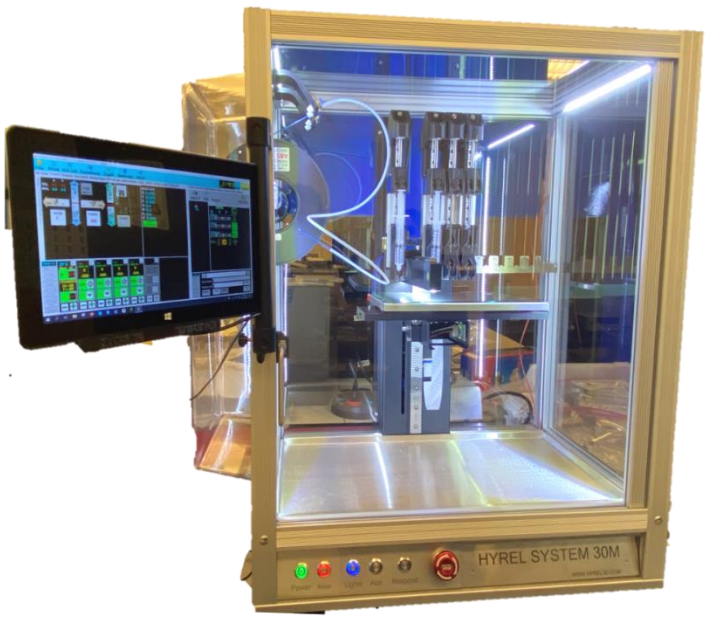

Figure 3.3. Image of the Hyrel 30M printer with modified print head used for the printing of the functional inks

3.4 Electrical Characterization of Printed Devices

After the device is printed out, the electrical transport properties and low-frequency electronic noise of the channel were investigated. The current-voltage characteristics of the device at constant and varying temperatures were measured using the cryogenic probe station (Lakeshore TTPX) with a semiconductor device analyzer (Agilent B1500). The sample was left in the chamber of the probe station and then the chamber was vacuumed down to a pressure of approximately 10^{-5} bar. The temperature can be adjusted by using a line of liquid nitrogen and a heater that are connected to the stage. The electronic noise setup includes a portable signal analyzer (Stanford Research 560) which was used for signal amplification when necessary. The voltage bias was supplied to the device using batteries to avoid the 60 Hz noise and its harmonics. More details of the measurements will be presented in the next chapters.

4 Printed Electronic Devices with Inks of TiS_3 Quasi-One-Dimensional Van der Waals Materials

4.1 Introduction

Recent years have witnessed a boost in printed electronics research and development as the technique facilitates mass production of electronic devices with lower cost and processing requirements [21,76]. The approach also enables the manufacturing of large-scale and flexible devices by expanding the choices of substrates from conventional silicon to flexible surfaces such as paper and textile [3,77,78]. Inks with proper thermophysical properties are the crucial component of the printing industry. Different functional materials have been developed and used as the ingredients for the inks employed by various printing techniques. Printed electronic devices can find applications in various areas. Flexible radio frequency tags,[79] wearable electronics,[77] organic light-emitting diodes,[80] and organic solar cells[81] are just a few examples of such applications. Despite the recent advancements, however, the list of available materials as ingredients for the inks is limited. Little is known about the nature of the charge transport and electronic noise characteristics in printed electronic devices.

Some of the previously demonstrated inks are based on metal nanoparticles, such as Ag,[15,16] Au,[17] and Cu,[18] carbon allotropes, such as graphene[19] and carbon nanotubes[82], and nanowires, such as ZnO, dispersed in suitable solvents.[1] Most recently the attention has turned to the layered quasi-two-dimensional (2D) van der Waals (vdW) materials, such as transition metal dichalcogenides (TMDs), including MoS_2,[22,23] $MoSe_2$,[21] WS_2,[24] and Bi_2Te_3.[25] The class of quasi-2D vdW materials is promising for printing owing to a relative ease of ink development. It is known that TMD materials have weak vdW bonding between structural units allowing for their exfoliation into flexible quasi-2D layers. The inks of quasi-2D vdW materials can be prepared by the liquid-phase exfoliation (LPE) process and dispersion of the exfoliated flakes in proper solvents. Additionally, TMDs exhibit tunable electronic and mechanical properties, which increase their value as ingredients for various functional inks.[34,83–87]

The class of layered vdW materials is not limited to quasi-2D materials only. Most recently, there was a rapid emergence of interest in vdW materials with quasi-one-dimensional (1D) crystal structures.[88,89] These materials are quasi-1D in the sense that they have strong covalent bonds along the atomic chains, and vdW bonds or substantially weaker covalent bonds in directions perpendicular to the chains [90–92]. Transition metal trichalcogenides (TMTs), with the chemical formula of MX_3, where M is a transition metal and X is a chalcogen, are a prominent group of quasi-1D vdW materials [90–93]. Examples of materials from this group include TiS_3, [94,95] $TaSe_3$, [90] NbS_3, [96] ZrS_3, [94,95,97,98] $ZrTe_3$,[99] and their solid solutions.[94] Unlike TMDs, which exfoliate into quasi-2D atomic planes, TMT crystals exfoliate into needle-like quasi-1D structures with high aspect ratios. [34,90,93,100]

Motivated by the recent developments in the quasi-1D vdW material synthesis and exfoliation, we demonstrate the feasibility of the use of such materials in the inks for printed electronics. The high aspect ratio and flexibility of the exfoliated bundles of quasi-1D atomic chains offer specific advantages: possibly better connectivity of the individual flakes, smaller loading fractions required to achieve electrical conduction. [101,102]

The intrinsic properties of quasi-1D vdW metals and semiconductors can add to the unique ink functionalities. The exfoliated quasi-1D TMTs have demonstrated exceptional electrical properties. For example, the bundles of TiS_3, $TaSe_3$, and $ZrTe_3$ have shown exceptionally high breakdown current densities of ~1.7 MA/cm^2, ~10 MA/cm^2, and ~100 MA/cm^2, respectively [31]For the present study, we selected TiS_3.[103–111] It is an n-type semiconductor with a bandgap of ~1 eV at room temperature (RT).[104,106,110–112] The material undergoes a metal – insulator transition at temperature $T_M \sim 220$ K and exhibits metal-like properties at higher temperatures.[113] Bulk TiS_3 whiskers were shown to have the RT Hall mobility of about 30 cm^{2}V^{-1}s^{-1},[107] and comparable exciton mobility of about 50 cm^{2}V^{-1}s^{-1}.[114] Theoretically, it has been suggested that a single quasi-1D monolayer of TiS_3 can have mobility of ~ 10,000 cm^{2}V^{-1}s^{-1}, which is higher than that of quasi-2D MoS_2.[115] The experimentally observed mobilities in TiS_3 are considerably lower than the theoretical prediction, likely due to the polar-optical phonon scattering.[113,116] The few-layer TiS_3-based field-effect transistors (FETs) revealed mobilities of about 20-40 cm^{2}V^{-1}s^{-1} and ON/OFF ratios of > 10^3;[34] these experimental values are comparable or higher than those in FETs based on few-layer MoS_2, which are ~10 to 20 cm^{2}V^{-1}s^{-1}.[32,33] On the other hand, it has been reported that TiS_3 exhibits charge-density-wave phase transitions at low

temperatures.[117] This feature, in addition to all other promising electrical characteristics, has made TiS_3 an interesting material to experiment with innovative inks for printed electronics. The use of quasi-1D TiS_3 can add new functionalities to the ink. A report on the LPE and drop-casting of TiS_3[118] suggested that this material might be suitable for ink printing if a proper solvent is found and printing parameters are optimized.

The crystal structure of monoclinic TiS_3 falls into the $P2_1/m$ space group. TiS_3 has a highly anisotropic structure, in which quasi-1D chains of TiS_3 prisms are covalently bonded along the *b*-axis. These weakly interacting chains are assembled into vdW-stacked quasi-2D layers parallel to the *ab* plane of the crystal structure. A previous theoretical study has shown that the cleavage energies required for breaking weak interactions between the quasi-2D layers separated by the vdW gaps and between the quasi-1D chains within the layers are both comparable to the cleavage energy of graphene layers in graphite.[93] Because of this, cleavage of TiS_3 crystals may realistically proceed along several different planes between the quasi-1D chains (such as (001), (100), (101), etc.), resulting in a formation of high-aspect-ratio exfoliated nanoribbons.[93]

Here we report on the fabrication and characterization of electronic devices printed with inks of quasi-1D van der Waals materials. The quasi-1D van der Waals materials are characterized by 1D motifs in their crystal structure, which allows for their exfoliation into bundles of atomic chains. The ink was prepared by the liquid-phase exfoliation of crystals of TiS_3 semiconductor into quasi-1D nanoribbons dispersed in a mixture of ethanol and ethylene glycol. The temperature-dependent electrical measurements indicate that electron transport in the printed devices is dominated by the electron hopping mechanisms. The

low-frequency electronic noise in the printed devices is of $1/f^{\gamma}$-type with $\gamma \sim 1$ near room temperature (f is the frequency). The abrupt changes in the temperature dependence of the noise spectral density and γ parameter can be indicative of the phase transition in individual TiS_3 nanoribbons as well as modifications in the hopping transport regime. The obtained results attest to the potential of quasi-1D van der Waals materials for applications in printed electronics.

4.2 TiS_3 Ink Preparation and Printed Device Fabrication

TiS_3 crystals were synthesized by the direct reaction between metallic titanium and a sulfur vapor in a vacuum-sealed quartz ampule at 550 °C, as described in our previous works.[34,114] (Figure 4.3(b)) Figure 4.1 presents the results of X-ray powder diffraction (XRD) measurements of the synthesized TiS_3 material. The TiS_3 crystals have been ground using an agate mortar and pestle and subjected to powder X-ray diffraction analysis using Cu Kα radiation. The pattern shows clear evidence of preferential orientation due to stacking of the material. The XRD pattern presented in Figure 4.1 along with its LeBail refinement demonstrates the high purity of the material. TiS_3 crystallizes in a $ZrSe_3$ – type structure with the $P2_1/m$ space group.[119] The lattice constants extracted by the LeBail analysis are a = 0.4965(1) nm, b = 0.3402(1) nm, c = 0.8801(1) nm, and β = 97.64(1); these values are in a good agreement with the previously reported data.[34,114,119] Because of their highly anisotropic crystal structure, these crystals are needle-shaped, with their long axes corresponding to the crystallographic b direction of the quasi-1D TiS_3 chains. The LPE

process was performed on these TiS_3 crystals in ethanol, resulting in cleavage of the bundles of the atomic chains, which appeared as needle-like nanoribbons. The liquid phase exfoliation was conducted by placing 100 mg of TiS_3 crystals in a round-bottom flask with 50 mL of dry ethanol. The round-bottom flask was sealed with a septum and then placed in the center of a 40 kHz ultrasonic bath sonicator. Nitrogen gas was bubbled through the dispersion during the first hour of sonication to remove any dissolved oxygen. The dispersion was sonicated for a total of 24 hours sealed under nitrogen gas. After exfoliation, the dispersion was transferred to a 20 mL dram vial. This transfer was conducted in a dry nitrogen-filled glove box to prevent any oxygen or water contamination. The resulting dispersion of the liquid-phase exfoliated TiS_3 in ethanol had a concentration of 2 mg/mL.

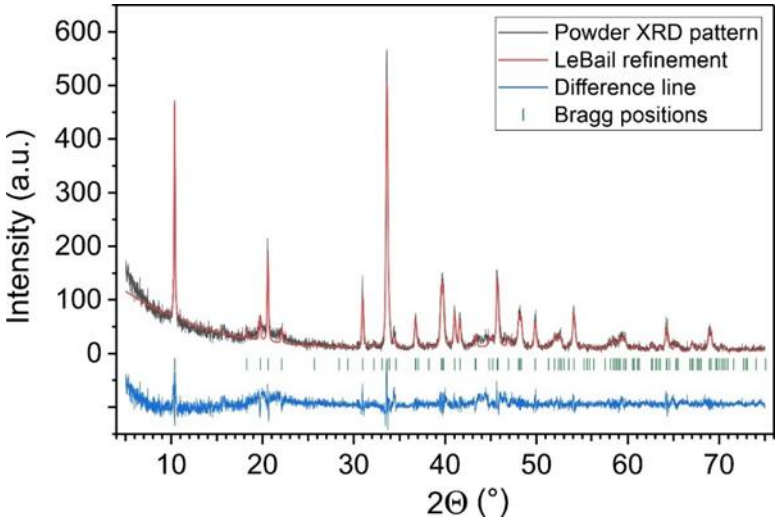

Figure 4.1 The powder XRD pattern of TiS_3 accompanied by the LeBail analysis.

The solution-exfoliated quasi-1D TiS_3 nanoribbons were characterized by atomic force microscopy (AFM). A droplet of TiS_3 dispersion in ethanol was placed on a Si/SiO_2

and dried in air. The resulting TiS_3 nanoribbons on a substrate were imaged using an atomic force microscope (Bruker Dimension Icon). The analysis of the AFM images was carried out using Gwyddion software.[120] A representative AFM image is shown in Figure 4.2(a). The solution-exfoliated TiS_3 particles generally had a ribbon-like shape, which is representative of the quasi-1D structure of TiS_3. The thickness of these nanoribbons varied from several hundred nm down to several nm as illustrated by the AFM height profile in Figure 4.2(b).

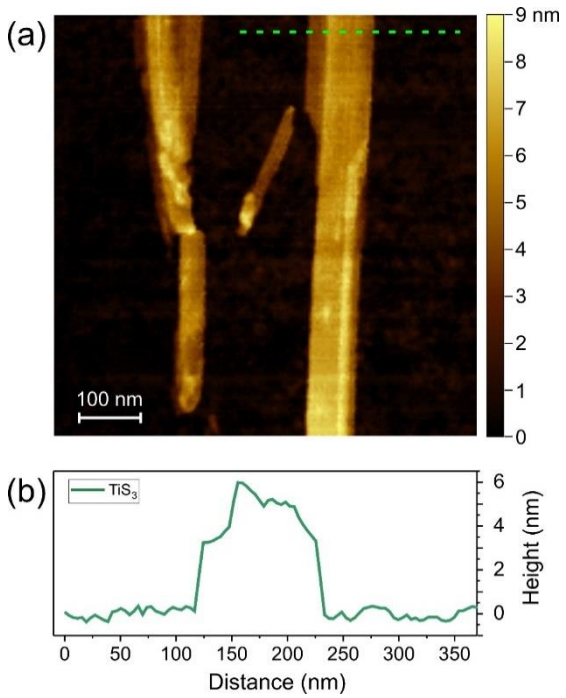

Figure 4.2. (a) Atomic force microscopy (AFM) image of the fragment of the TiS_3 nanoribbons on Si/SiO_2 after the liquid phase exfoliation. (b) AFM thickness profile measured along the green dashed line across one of the solution-exfoliated TiS_3 nanoribbons in panel (a). Reprinted with permission from Supporting Information of Baraghani et al., Printed electronic devices with inks of TiS_3 quasi-one-dimensional van der Waals material, ACS Appl. Mater. Interfaces. 13 (2021) 47033–47042. Copyright (2021) American Chemical Society.

The quality of the material after the exfoliation has been confirmed with Raman spectroscopy (Renishaw InVia). The measurements were performed in the backscattering configuration under a visible red laser ($\lambda = 633$ nm). The laser spot size on the sample was ~1 μm. The excitation power on the sample's surface was varied between 0.1 μW and 2 mW. After each measurement, the samples were carefully inspected using optical microscopy. No laser-induced changes in the samples were detected. Figure 4.3(c) presents the Raman spectrum of exfoliated TiS_3 bundles at RT. The monoclinic structure of TiS_3 has C_{2h} point symmetry with the irreducible representation of $\Gamma = 8A_g + 4B_g + 8B_u + 4A_u$. Four dominant Raman peaks identified at 174, 297, 367, and 556 cm^{-1} belong to A_g vibrational symmetries.[92,93,121] The peak at 174 cm^{-1} is associated with the rigid chain vibrations.[121] The two peaks at 297 cm^{-1} and 367 cm^{-1} are related to the internal out-of-plane vibrations involving each monolayer. The peak at 556 cm^{-1} is attributed to S – S diatomic motions.[121] The three low-intensity peaks at 163, 276, and 401 cm^{-1} that shoulder to the dominant Raman peaks belong to B_g vibrational symmetries.[122,123] The Raman spectra confirm the material quality after the exfoliation processing steps. To further confirm the high quality and crystallinity of the solution-exfoliated TiS_3 nanoribbons, we studied them by transmission electron microscopy (TEM) (FEI Tecnai Orisis). The accelerating voltage was 200 kV. TEM image of a representative TiS_3 nanoribbon is shown in Figure 4.3(d). A selected area electron diffraction (SAED) pattern recorded on this nanoribbon (see the inset in Figure 4.3(d)) confirms that it is highly crystalline. According to the indexing of the diffraction spots in this SAED pattern, the observed view corresponds to the *ab* plane of TiS_3. The long axis of the crystal represents the crystallographic *b*

direction of the quasi-1D chains, which is in agreement with the most expected exfoliation scenario.[93] A high-resolution TEM image in Figure 4.3(e), which was recorded for the same nanoribbon, confirms that this is the *ab* plane, because the observed interplanar distances perfectly match the *a* and *b* crystal structure parameters of TiS_3 (a = 0.4948 nm, b = 0.3379 nm, c = 0.8748 nm, and the cant angle β = 97.62°).

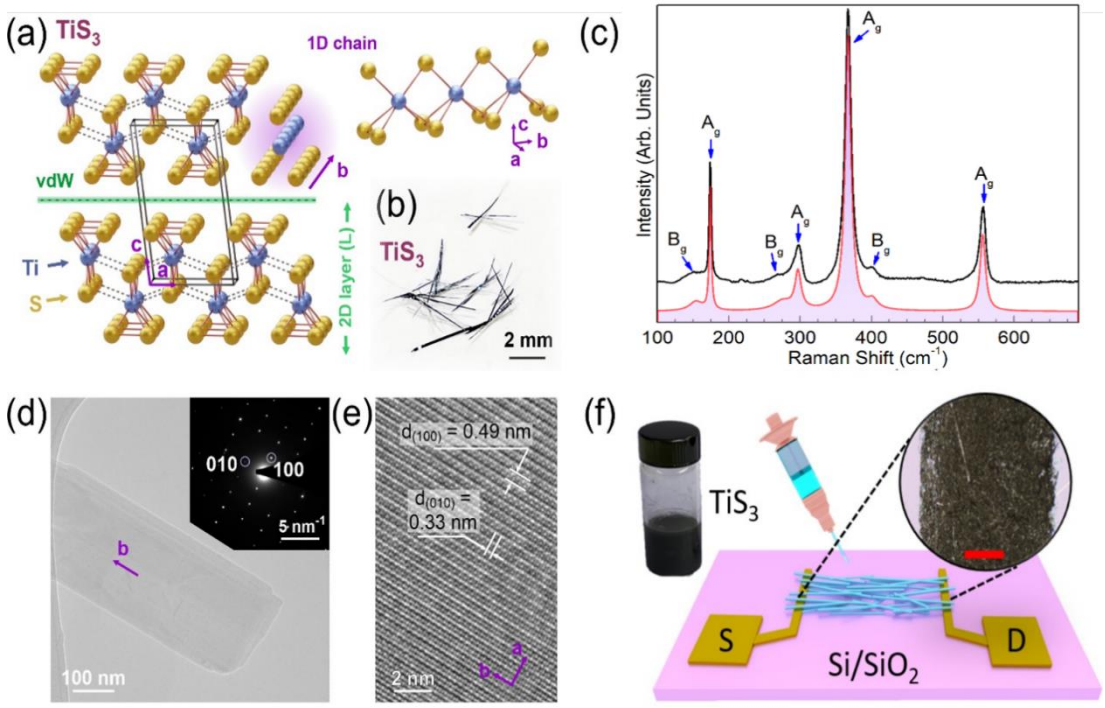

Figure 4.3. (a) Schematic of the monoclinic crystal structure of TiS_3 from two viewpoints. The blue and yellow spheres represent the Ti and S atoms, respectively. The parallelogram demonstrates the unit cell of TiS_3. The side view in the right panel exhibits the quasi-1D nature of the atomic chains. (b) Optical photograph of the TiS_3 crystals used in this study. (c) Raman spectrum of exfoliated TiS_3 (black curve) at room temperature. The red curve shows the cumulative fitting of the experimental data by individual Gaussian functions. (d) TEM image of a representative solution-exfoliated TiS_3 nanoribbon. A SAED pattern recorded on this crystal is shown in the inset. (e) High-resolution TEM image of the same TiS_3 nanoribbon as in panel (d). (f) Schematic of the printing process of TiS_3 devices on top of gold contacts made with electron beam lithography. The image in the dashed circle is the optical image of the actual TiS_3 device channel. Note the absence of the "coffee-ring" effect in the channel confirming that the material is distributed evenly. The scale bar is 200 μm. The vial contains the liquid-phase exfoliated TiS_3 ink. Reprinted with permission from Baraghani et al., Printed electronic devices with inks of TiS_3 quasi-one-dimensional van der Waals material, ACS Appl. Mater. Interfaces. 13 (2021) 47033–47042. Copyright (2021) American Chemical Society.

A schematic of the printing procedure and device is shown in Figure 4.3(f). The electrodes were fabricated by e-beam lithography followed by the lift-off of Ti/Au (20-nm/200-nm) deposited by e-beam evaporation. The TiS_3 channel was printed by a 3D

printer (Hyrel 30M) on top of the electrodes. To mimic the function of an inkjet printer, the printer head was swapped with a syringe holder and a syringe was utilized for dispensing of the ink. A blunt-end needle syringe with gauge 27 was used with the printer. 20 layers of material were printed on the substrate with the gold electrodes. The printed channel has the dimensions of 500 μm×4 μm×6 μm (W×L×t). The thermophysical properties of the ink and proper selection of the injecting nozzle size play a crucial role in the ink droplet formation, even spreading of the ink on the substrate and subsequent drying. The nonuniform deposition of the material in printing often happens as a result of the "coffee-ring" effect that should be avoided by adjusting the concentration of the ingredients in the ink and surface modification of the substrate.[124] The droplet formation behavior is characterized by a dimensionless Z-number (inverse of Ohnesorge number)[59,125], $Z = \sqrt{\zeta \rho a}/\mu$, where a is the printer's nozzle diameter [m], and ζ, ρ, and μ are the surface tension [N m^{-1}], density [kg m^{-3}], and dynamic viscosity [Pa × s] of the ink, respectively. Generally, proper droplet formation and dispense occur in the range of $1 \leq Z \leq 14$. Otherwise, satellite droplet formation ($Z > 14$) or elongated ligaments ($Z < 1$) may deteriorate the accuracy of the printing by deposition of the ink on undesired areas.[43,50,58,59]. However, there are studies that report quality printings with $Z \geq 14$, especially for nanomaterial-based inks. For example, graphene-based inks with $Z \sim 24$ or polystyrene-nanoparticle-based inks with $Z \sim 21$ to ~ 91 have been successfully printed.[44,50,126–128] Therefore, the Z-number limits seem not to be strict for vdW materials, and inks with Z-number values close to the range guarantee proper printing quality.

To tune the Z-number for printing with quasi-1D vdW ink, we used a syringe with an inner diameter of $a = 210$ μm. 3 mL of 4 mg/mL of exfoliated TiS_3 in ethanol was mixed with 3 mL of ethylene glycol (EG) to give 6 mL of 2 mg/mL of TiS_3 in 1/1 vol% ethanol/ethylene glycol as the ink. Ethylene glycol was added to the ink to increase the viscosity of the ink. This is to ensure proper dispensing and drying of the ink. The viscosity, surface tension, and density of the ink were measured to calculate the characteristic Z number. To measure the viscosity, a Cannon SimpleVIS viscometer was used. 0.5 μL of the ink was inserted into the device and the measured kinematic viscosity was displayed on the device screen. Then this value was divided by density to calculate the dynamic viscosity. A CSC Scientific DuNouy interfacial tensiometer was used to calculate the surface tension of the ink. To measure the surface tension, the device ring was inserted into the ink. Then, the ring was raised slowly until the film between the ink and the ink breaks, and the measured amount of surface tension can be read from the device dial. With the addition of EG to the ink, the dynamic viscosity and surface tension of the ink were measured to be $\zeta \sim 3.3\ [\mathrm{Nm}^{-1}]$ and $\mu \sim 3.35 \times 10^{-3}\ [\mathrm{Pa} \times \mathrm{s}]$, respectively. The mass density of the ink was calculated using the rule of density for mixtures. The calculated density of the ink was $\rho \sim 949.6\ [\mathrm{kgm}^{-3}]$. With these values, the calculated Z number of the ink is $Z \sim 24$ for the nozzle with inner diameter of 210 μm used in this work. No satellite droplet formation or elongated ligaments were observed during the printing. The addition of EG helped to circumvent the "coffee-ring".[60] This is depicted in Figure 4.4. A faster evaporation rate of ethanol causes enrichment of the droplet contact line with EG, leading to a surface tension gradient in the droplet and uniform dispersion of the material while

drying.[43,76] As seen, the addition of EG results in the elimination of the coffee-ring effect. To augment the flow through the ink droplet the bed temperature of the printer was kept at 60 ^{o}C.

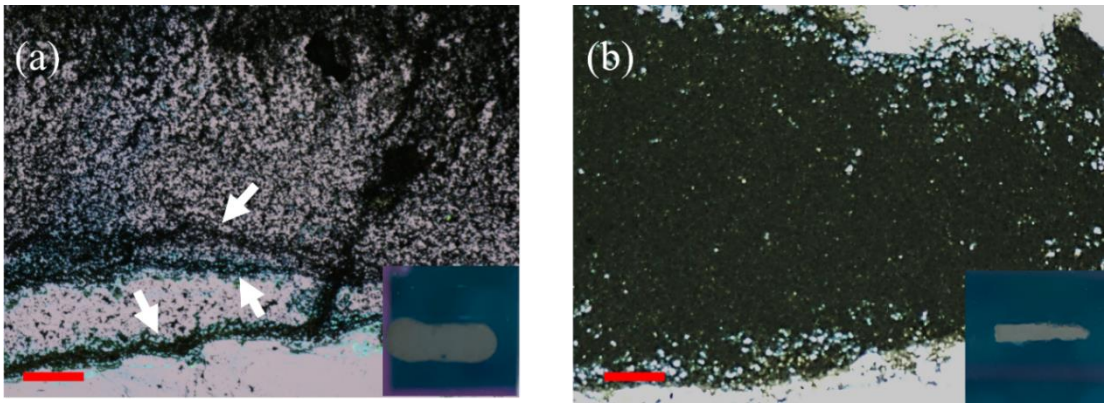

Figure 4.4. Optical image of the printed line (a) before, and (b) after the addition of ethylene glycol. The scale bar is 200 µm. Heavy formation of coffee-rings can be observed in the printed trace before addition of EG. These are marked with arrows in the image. In addition, the width of the printed line is larger than when ethylene glycol is added. Reprinted with permission from Supporting Information of Baraghani et al., Printed electronic devices with inks of TiS_3 quasi-one-dimensional van der Waals material, ACS Appl. Mater. Interfaces. 13 (2021) 47033–47042. Copyright (2021) American Chemical Society.

Figure 4.5 (a) shows an SEM image of the channel. As seen, the printed channel has the dimensions of 500 µm×4 µm×6 µm (L×W×t). The average thickness of the device was measured using an optical profilometer (Figure 4.5 (b)).

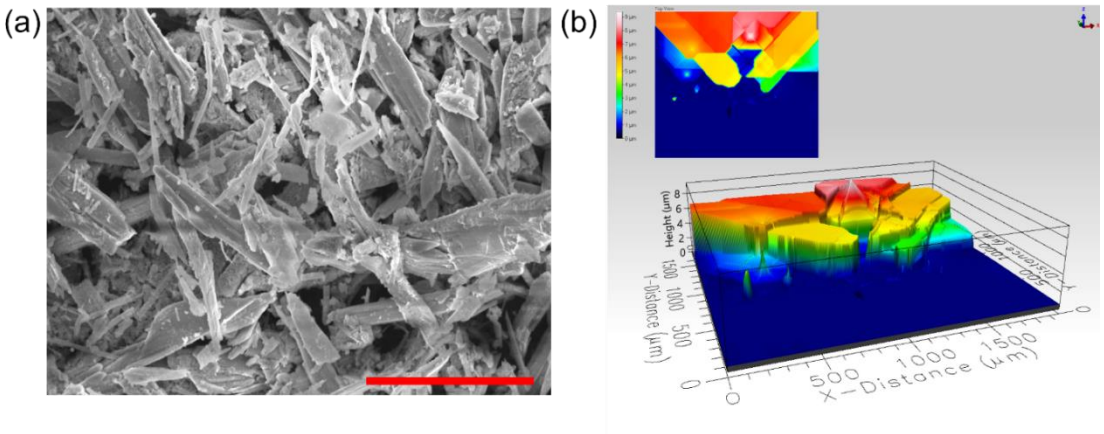

Figure 4.5. (a) SEM image of the printed device channel showing the quality of the material exfoliation and the morphology of nanoribbons in the ink and in the printed channel. The scale bar is 10 µm. (b) Surface profile of the printed channel. The roughness of the surface and the thickness of the film can be determined from this data. The inset is the top view of the channel surface profile. Reprinted with permission from Supporting Information of Baraghani et al., Printed electronic devices with inks of TiS_3 quasi-one-dimensional van der Waals material, ACS Appl. Mater. Interfaces. 13 (2021) 47033–47042. Copyright (2021) American Chemical Society.

4.3 Electrical Characterization and Low-Frequency Noise Measurements

All current–voltage (I–V) characteristics and resistivities were measured in the cryogenic probe station (Lakeshore TTPX) with a semiconductor analyzer (Agilent B1500). The low-frequency noise experiments were conducted in the two-terminal device configuration. The noise spectra were measured with a dynamic signal analyzer (Stanford Research 785). A battery biasing circuit was used to apply a bias voltage to the devices. This was done to minimize the noise at 60 Hz and the harmonics associated with it. The signal measured by the dynamic signal analyzer is the absolute voltage noise spectral density, S_v, of a parallel resistance network consisting of a load resistor (R_L) of 46 KΩ and

the device under test with a resistance of R_D. The normalized current noise spectral density, S_I/I^2, was calculated $S_I/I^2 = S_V \times [(R_L + R_D)/(R_L \times R_D)]^2/(I^2 \times G)$ where G is the amplification of the low-noise amplifier.

4.3.1 Electrical Transport Characterization

The electrical current-voltage (I-V) characteristics of the fabricated two-terminal devices were measured in the temperature range from 78 K to 350 K. The I-V results are presented in Figure 4.6(a). The weakly non-linear I-V curves were attributed to formation of the Schottky barrier at the printed channel – metal contact interface. Interestingly, it was previously shown that Au forms an Ohmic contact with TiS_3,[129] provided that there is a clean ultrahigh-vacuum-enabled interface between the two materials resulting in strong Au-S interactions. The presence of Schottky barrier for these devices can be explained by the fabrication process, where the interfaces between the printed TiS_3 nanoribbons and the Ti/Au pads contain various surface adsorbates and residual solvent molecules. At low bias voltage, from -0.1 V to 0.1 V, the I-V characteristics can be considered approximately linear (see the inset to Figure 4.6(a)). The resistivity of the printed TiS_3 channel was extracted a standard two-probe technique (see Figure 4.6(b)). The resistance, R, was extracted from the linear part of the I-V plots presented in Figure 4.6(a). Assuming the isotropic properties in all directions, the resistivity was determined from the formula $\rho = RA/l$, where l and A were the channel length and the cross-sectional area, respectively. At RT, the resistivity of the printed devices was ~195 Ω×m. The resistivity values reported in

the literature span a wide range from 0.02 Ωm to 200 Ω×m for individual exfoliate bundles of atomic chains, *i.e.* nanoribbons, and crystals with defects.[113,117,118] Note that our resistivity results include the contact resistance. The solvent residues can also affect the overall resistance of the channel. Given the disordered nature of the printed device, the extracted values of resistivity are reasonable and consistent with data reported for individual nanoribbons.[113]

As one can see in Figure 4.6(b), the resistivity continuously decreases with increasing temperature. This is in contrast with the data on the electrical resistivity measurements of bulk and mechanically exfoliated few-layer TiS_3 devices reported over an extended temperature range of 4 K to 400 K. [104,107,108,113]. In the latter case, the resistivity decreased with the temperature increasing up to ~250 K, which is typical for semiconductor material. At temperatures above 250 K, TiS_3 exhibits metallic properties, *i.e.* the resistivity increases with the temperature rise.[113] In printed devices, however, one would expect to have a network of randomly arranged exfoliated TiS_3 atomic chain bundles with many bundle to bundles interfaces, defects, and impurities resulting from the LPE process and subsequent printing. In this case, the electron hopping transport to be the main mechanism of electron conduction. The electrically conductivity due to electron hopping has smaller values than the bulk band conduction, and it increases with increasing temperature. We now analyze the resistivity data in more details.

Several models have been proposed to describe the electron hopping in disordered material systems[130]. In the nearest neighbor hoping (NNH) model, the system is considered to have randomly distributed isoenergetic sites with a concentration of N_0 and the electron

localization length of α so that $N_0\alpha \ll 1$. The electrical conduction is carried out by the charge carriers jumping between the nearest sites. The temperature dependence of the electrical conductivity in NNH mechanism, σ_{NNH}, is described by the equation $\sigma_{NNH} = \sigma_{0NNH}\exp(-E_{NNH}/k_BT)$, where k_B is Boltzmann constant, σ_{0NNH} and E_{NNH} are the NNH conductivity constant and the NNH activation energy, respectively. This equation is similar to the equation for the electrical conductivity in the thermally activated band-conduction model, $\sigma = \sigma_0\exp(-E_a/k_BT)$, where E_a is the thermal activation energy. The main difference in the formalisms is that $E_{NNH} < E_a$ so that generally NNH occurs at rather high temperature where the thermal activation energy is not sufficient to excite electrons to the conduction band but enough to excite them to the available spatially-separated energy sites between the conduction and valence bands. At the low-temperature limit, the electron hopping is dominated by the variable-range hoping (VRH) mechanism[130–134] where the upward transition of electrons between energetically distinct but spatially nearby states is less likely than the transition to states with energetically close but spatially farther away states. Our experimental data at low temperature can be better described with the Efros-Shklovskii VRH model[130,131,134] in which the hoping distance between the trap sites is not constant and carriers can hop between the levels closer to the Fermi level.[131] The temperature-dependent conductivity in this model is described by the equation $\sigma = \sigma_{0ES}\exp[-(T_{ES}/T)^{1/2}]$, where σ_{0ES} and T_{ES} are parameters that depend on the localization length and dielectric constant of the material.[134]

Figure 4.6(c) shows the Arrhenius plot of the resistivity data in the entire examined temperature range.[131,135] The plot is divided into four regions shaded in yellow, blue,

orange, and green colors. The blue and green regions correspond to the temperature ranges where the slope of the resistivity changes significantly. The change in the slope of the curve in blue region is a signature of transitioning from VRH (yellow) to NNH (orange) conduction in disordered materials.[132,136–139] The activation energy calculated for the NNH conduction is ~12.4 meV. As expected, the extracted value is significantly lower than the thermal activation energy reported for bulk TiS_3 crystals which is ~43 meV.[105,107,113] The data deviates from the NNH model at high temperature again (see green area in Figure 4.6(c)). The reason for such a deviation needs a further investigation. Some previous studies have reported that bulk crystals of TiS_3 are likely to undergo the charge density wave (CDW) phase transitions at ~60 K and ~220 K.[113,117] The high-temperature phase transition in bulk form can happen in the temperature range between 200 K to 260 K, depending on the quality of the sample.[117] The reported phase transition temperatures are close to the transition regions, which we marked in green and blue colors in Figure 4.6(c). Figure 4.6(d) shows the resistivity data as a function of $T^{-1/2}$ in the temperature range from 78 K to 115 K where VRH conduction dominates. According to the Efros-Shklovskii VRH model, the plot of $\ln(\sigma)$ as a function of $T^{-1/2}$ must be linear. One can see an excellent agreement between our experimental data and the fitted linear regression in this temperature range.

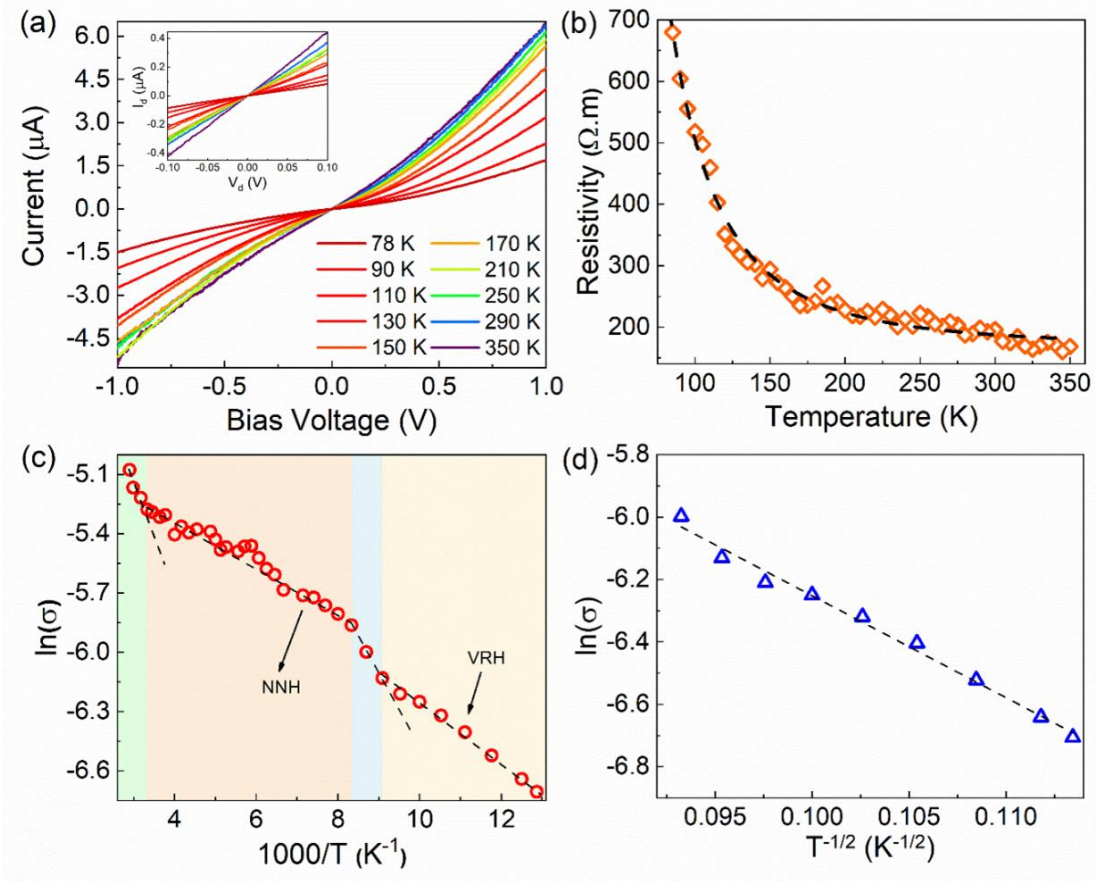

Figure 4.6. (a) Current-voltage characteristics of the TiS_3 printed device as a function of temperature. The inset shows the linear I-V dependence at small bias voltages. At higher voltages, the I-V curves become non-linear. (b) Electrical resistivity of the printed TiS_3 channel as a function of temperature. The decrease in resistivity with temperature increase is consistent with the electron hopping transport mechanism. (c) Arrhenius plot of the electrical conductivity of the printed TiS_3 channel. Different shades of color in the plot indicates changes in conduction mechanism from nearest-neighbor hopping (NNH) to variable-range hopping (VRH). (d) Plot of $\ln(\sigma)$ versus $T^{-1/2}$ for the printed device channel at low tempratures. The experimental data agrees with the theoretical Efros - Shklovskii variable range hoping model (dashed line). Reprinted with permission from Baraghani et al., Printed electronic devices with inks of TiS_3 quasi-one-dimensional van der Waals material, ACS Appl. Mater. Interfaces. 13 (2021) 47033–47042. Copyright (2021) American Chemical Society.

4.3.2 Low-Frequency Noise Experimental Results

We used the low-frequency electronic noise spectroscopy to further elucidate the electron transport properties in our printed devices. The details of our experimental setup and measurement procedures have been reported elsewhere in the context of other material systems [63,138]. The analysis of the noise spectral density, its functional dependence on frequency, electric bias and temperature can provide a wealth of information on electron transport, particularly in material systems with high concentration of defects and impurities which act at the charge trapping sites. We have successfully used the electronic noise spectroscopy for monitoring phase transitions in materials which reveal strongly correlated phenomena [29,62,138,140,141] Typically, at the frequencies f<100 kHz, materials show the spectral noise density of $S(f) \sim 1/f^{\gamma}$ type, with $\gamma \sim 1$. In Figures 4.7(a) and (b) we present the voltage-referred noise power spectral density, S_v, and the normalized current noise power spectral density, S_I/I^2, for the device channel printed with the quasi-1D TiS_3 ink as a function of frequency. The noise spectra were measured for several bias voltages at RT. One can see that the noise generally follows the $1/f$ trend, and it increases with the increase in bias voltage as expected [62,138,141]. There are some traces of Lorentzian-type bulges at frequencies above f=100 Hz. They can indicate a presence of certain defects or impurities with particularly high concentration that act as the trapping centers for the charge carriers contributing to the current conduction. If such a defect, with a characteristic time constant of the charge carrier trapping and de-trapping, dominates the current fluctuations, its contribution to noise spectrum appears as a Lorentzian bulge.[142]

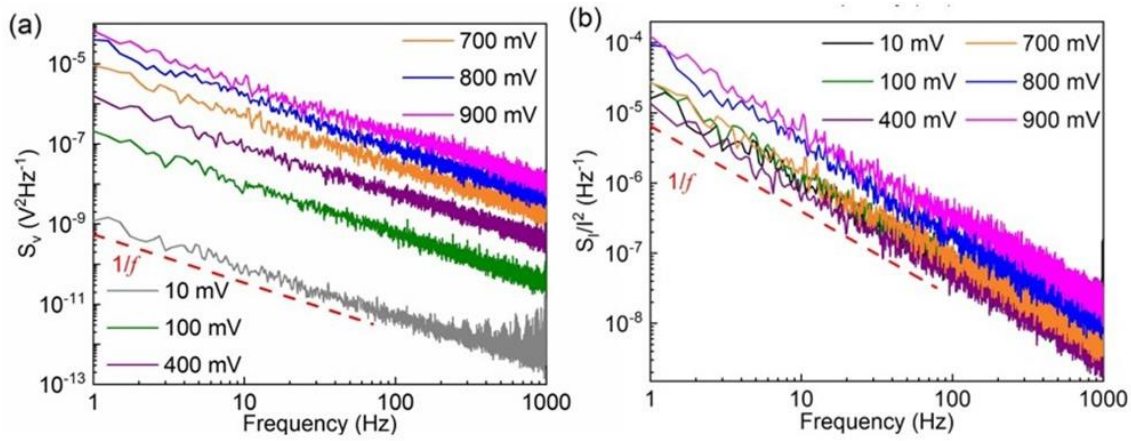

Figure 4.7. (a) Voltage-referred noise power spectral density, and (b) the normalized current noise power spectral density as the function of frequency at different applied bias voltages. The data in (a) and (b) follows $1/f$ noise dependency. Reprinted with permission from Baraghani et al., Printed electronic devices with inks of TiS_3 quasi-one-dimensional van der Waals material, ACS Appl. Mater. Interfaces. 13 (2021) 47033–47042. Copyright (2021) American Chemical Society.

Figures 4.8(a) and (b) show the voltage noise spectral density, S_v, and the normalized current spectral density, S_I/I^2, as a function of temperature. All measurements were carried out with a small applied bias of ~0.3 V to avoid Joule heating. The spectra in both plots follows the $1/f^{\gamma}$. However, γ is no longer close to 1, and it reveals a rather strong functional dependence on temperature. Figure 4.8(c) shows the extracted values of γas a function of temperature in the range from 130 K to 350 K. The black dashed lines are eye guides only. The observed large deviation of γ from 1 can be related to the Lorentzian bulges (see Figure 4.8(a) and (b)), which are more pronounced at low and high temperature limits. The changes in the noise spectra can be associated with the reported metal – insulator transition at temperature T_M~250 K [113] as well as the change in the

electron hopping conductivity around T~320 K (see green region in Figure 4.6(c)). Figure 4.8(d) shows the normalized noise spectral density, S_I/I^2, as a function of temperature at the fixed frequency of 10 Hz. The noise level abruptly increases at the temperature of ~320 K. This supports the hypothesis of changes in the electron hopping transport mechanism as seen in resistivity data in Figure 4.6(c) and γ parameter dependence in Figure 4.8(c).

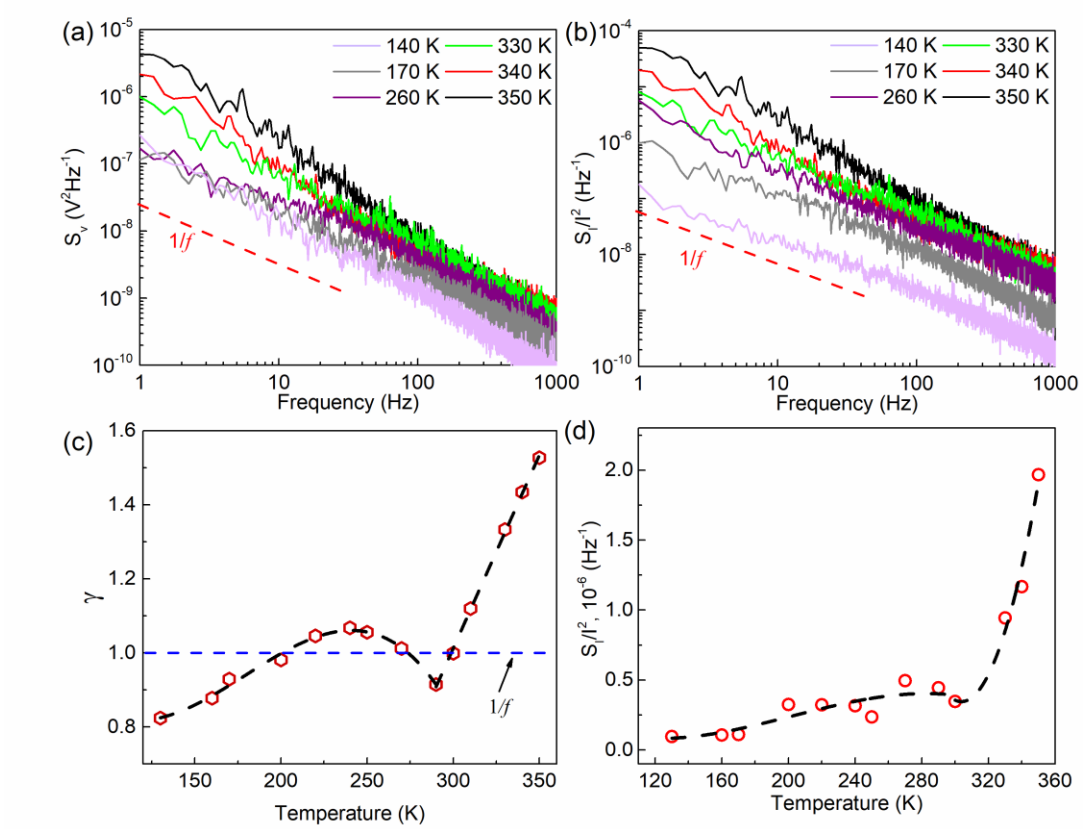

Figure 4.8. (a) Low-frequency noise spectra of voltage fluctuations, S_v, as a function of frequency measured at different temperatures. (b) Normalized current noise spectral density as a function of frequency for various temperatures. (c) Extracted values of γ as a function of temperature. (d) Normalized noise spectral density versus temperature at the constant frequency of $f = 10$ kHz. Reprinted with permission from Baraghani et al., Printed electronic devices with inks of TiS_3 quasi-one-dimensional van der Waals material, ACS Appl. Mater. Interfaces. 13 (2021) 47033–47042. Copyright (2021) American Chemical Society.

4.4 Conclusions

In conclusions, we reported on printing electronic devices with inks of quasi-1D vdW materials. The ink was prepared by the LPE of small crystals of TiS_3 semiconductor into quasi-1D nanoribbons dispersed in a mixture of ethanol and ethylene glycol. The temperature dependent electrical measurements indicate that electron transport in the

printed devices is dominated by the electron hopping mechanisms. The low-frequency electronic noise in the printed devices is of $1/f^{\gamma}$-type with $\gamma \sim 1$ near room temperature (f is the frequency). The abrupt changes in the temperature dependence of the noise spectral density and γ parameter can be indicative of the phase transition in individual TiS_3 nanoribbons as well as modifications in the hopping transport regime. The obtained results attest to the potential of quasi-1D vdW materials for applications in printed electronics. The developed printing process can also facilitate characterization of new quasi-1D van der Waals materials predicted by the machine learning studies, which are being currently synthesized.

5 Charge-Density-Wave Inkjet Printed Devices with Solutions of 2D van der Waals Materials

5.1 Introduction

Solution-processed two-dimensional (2D) van der Waals materials offer a scalable route toward the next-generation of printed electronics on flexible substrates. The inks of 2D materials are essential for wearable and skin electronics based on mechanically soft and stretchable materials allowing for integration with the human body.[1,143–147] Inkjet printing is one of the most promising approaches for large-area fabrication of flexible electronics. Printing of a wide range of electronic components, including metal wiring and interconnects, field-effect transistors, photovoltaic devices, and light-emitting diodes, has been demonstrated. The inkjet printing is based on a limited number of process steps, and as such, well suited for mass production. However, there is one serious issue with the printed electronics that utilize the inks of 2D van der Waals materials. One can readily print a metallic conductor or an electrical insulator. A percolated network of graphene or metallic carbon nanotubes can conduct the electricity efficiently, offering a rather low sheet resistance.[20,82,148] A printed layer with an ink of boron nitride flakes can serve as an efficient

electrically insulating barrier, serving, for example, as a gate dielectric. Unfortunately, a printed layer with the ink of semiconducting flakes never offers an electrical conductivity characteristic of the true band-conduction semiconductor. The reason is that in any printed channel with the ink of semiconducting materials, *e.g.* MoS_2, the electrical conductivity will be of the electron hopping type, having little to do with the intrinsic semiconducting properties of the 2D material used in the ink. This explain why the electron mobilities in the most of the printed transistors are below 10 $cm^2V^{-1}s^{-1}$, and in many cases are below 0.5 $cm^2V^{-1}s^{-1}$. Some approaches that let to mobilities above 10 $cm^2V^{-1}s^{-1}$ require extra processing steps, utilize nanoparticle inks are not stable in ordinary solvents, yet still do not attain the band-type conduction. We deal with a fundamental problem - one cannot achieve the semiconducting band conduction transport in printed device channels. In any percolated network of semiconducting flakes, the electron transport will be limited by the interface between the two contacting flakes. In order to overcome this challenge which limits the applications of printed electronics one has to come up with an unconventional solution.

Recently, charge-density-wave (CDW) materials and devices attracted renewed interest in the context of 2D van der Waals materials.[27,29,61,64,149–151] The 1T polymorph of TaS_2 is one of 2D van der Waals materials of the transition-metal dichalcogenide (TMD) group that reveals several CDW phase transitions in the form of resistivity changes and hysteresis.[152,153] A schematic of the crystal structure of the material is presented in Figure 1.a. The transitions can be induced by temperature and electric bias.[64,140,151] The phase transitions at ~200 K and 350 K are accompanied by a pronounced hysteresis in the current-

voltage response. It is worth mentioning that the transition at lower temperature cannot be observed if the thickness of the material is too small. At temperatures below this lower transition (~200 K), the charge density is fully commensurate with the underlaying lattice (C-CDW). At this state, the atoms form aggregates of 13 atoms in the form of start of David as exhibited in Figure 5.1(a). As the temperature increases, the material enters a nearly commensurate phase (NC-CDW) in which islands of commensurate phase exist in a sea of incommensurate phase. This is demonstrated in Figure 5.1(b). Continuation of temperature increase will drive the material to the incommensurate (IC-CDW) phase at temperatures higher than 350 K as shown in Figure 5.1(c). The hysteresis associated with the transition from the nearly commensurate (NC) CDW phase to the incommensurate (IC) CDW phase at 350 K has been already exploited in a number of demonstrated devices with the micrometer scale channels.[151] Here, we use the ink of 1T-TaS_2 van der Waals material to print the CDW device. Since the functionality of the device is based on the hysteresis, which happens in each individual flake of 2D material, it is not impeded by the interfaces between the percolating flakes. In this printed CDW device we do not rely on the electron hopping conductivity but rather on the change in the resistive state in the flakes contained in the ink. Our approach allows to achieve the same intrinsic functionality in the large-area printed devices that is available in the individual 1T-TaS_2 channels. It constitutes a game changer for printed electronics and overcomes the problem of inability to print a semiconducting channel for achieving certain functionalities.

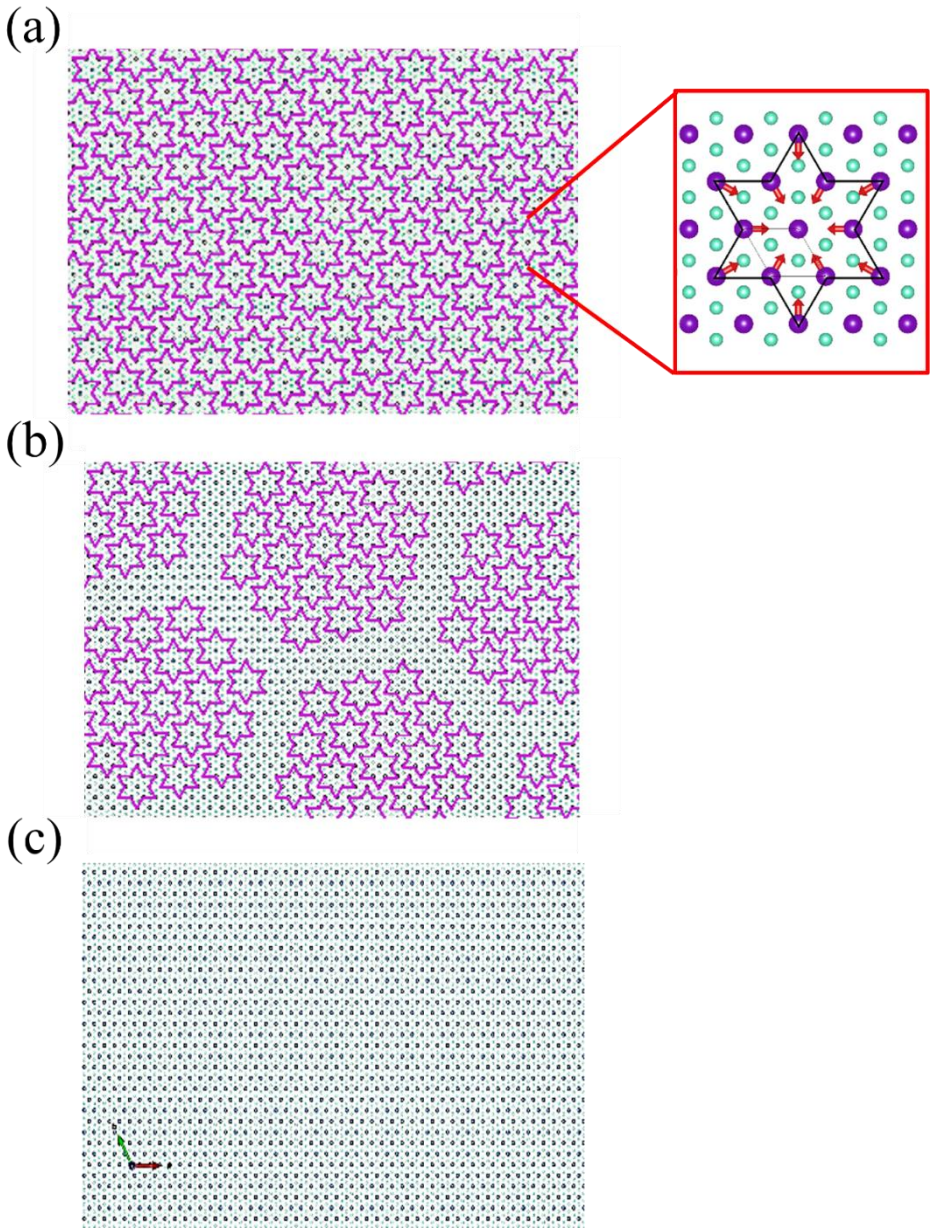

Figure 5.1. Schematics of 1T-TaS_2 atoms in (a) fully commensurate CDW phase, (b) nearly commensurate CDW phase, and (c) incommensurate CDW phase

5.2 1T-TaS_2 Ink Preparation

5.2.1 Crystal Synthesis

High-quality 1T-TaS_2 used for this study was synthesized by the chemical vapor transport (CVT) method from the elements using I_2 as the transport agent through quenching from the crystal growth temperature. The details of the synthesis process is reported elsewhere.[149,154,155] Optical and SEM images of the crystals are presented in Figure 5.2 (a-b). Raman spectroscopy on the crystals was carried out at room temperature to further confirm the quality of the crystal (Figure 5-2 (c), purple curve). There are six Raman peaks observed at 64, 98, 239, 310, 367, and 390 cm^{-1}. The spectral position of these peaks agrees well with the Raman signature of TaS_2 previously reported in the literature.[156–162]

5.2.2 Liquid Phase Exfoliation of 1T-TaS_2

The synthesized 1T-TaS_2 crystals were exfoliated in the DMF solvent. 3 mg of the bulk crystals were placed in a vial containing 10 mL of DMF. The mixture was sonicated in a bath sonicator for 90 minutes. After this step, some unexfoliated parts of the crystal were removed from the solution and sonicated in 5 mL of DMF for another 90 minutes. The procedure was repeated until no unexfoliated crystals were left. Raman spectrum of the exfoliated flakes are shown in Figure 5.2(c). As seen, the spectral position of the Raman peaks of the exfoliated material matches that of the as-grown crystal. However, there is a

broadening of the peak located at 64 cm^{-1}, most likely due to the defects introduced to the crystal during the LPE process.[158]

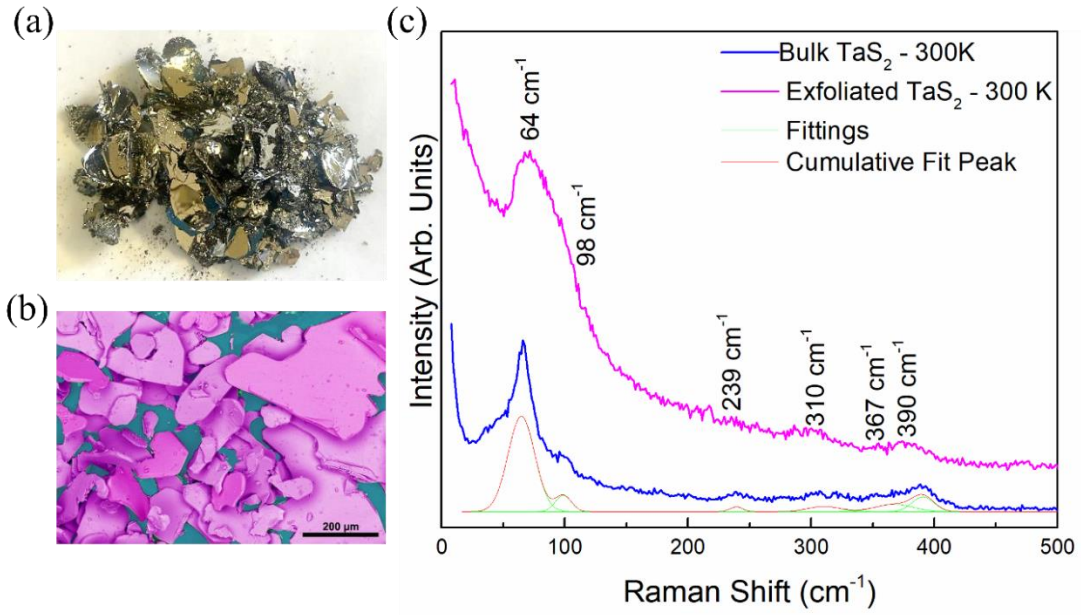

Figure 5.2. (a) Optical, and (b) SEM images of the synthesized 1T-TaS_2 crystals. (c) Raman spectra of the bulk 1T-TaS_2 crystal at room temperature before (purple curve) and after (blue curve) liquid phase exfoliation. The green and red lines are the individual and cumulative Gaussian fittings of the Raman peaks in blue curve.

5.2.3 Ink Preparation

The exfoliated 1T-TaS_2 flakes were then transferred and redispersed in isopropyl alcohol to facilitate faster drying of the ink droplets during the printing process. For the solvent exchange process, the solution was centrifuged at 11000 rpm for 15 minutes to separate the exfoliated flakes from the DMF. The DMF was then removed and the exfoliated flakes were dispersed in 10 mL of IPA as the secondary solvent. The solution

was sonicated for 5 minutes to ensure good dispersion of the exfoliated material and to eliminate any possible agglomeration of the exfoliated flakes. This step was repeated three times to remove any excess DMF that might have been left in the solution. The exfoliated flakes were sorted based on the thickness and lateral size using centrifugation at different speeds. In this method, the solution was centrifuged at 3000, 5000, and 8000 rpm for 30 minutes leading to large, medium, and small flakes separated. The centrifugation process was started at 3000 rpm and at each time, the supernatant was collected. The sediments were dispersed in 5 mL of IPA:EG (1:1 vol%) as the final ink formulation. Note that, as described previously, EG was added to tune the viscosity and drying rate of the ink and will be explained in more details next.

5.2.4 Thermophysical Properties and Printing Parameters of the Ink

As described in the previous chapter, the thermophysical properties of the ink as well as the printing nozzle diameter determines the Z-number (Equation 2-2). Typically, for the printing process, the Z-number should be in the range of $1 \leq Z \leq 14$ or otherwise, satellite droplet formation ($Z > 14$) or elongated ligaments ($Z < 1$) may occur. This is problematic as it can drastically reduce the print quality by having inks drop at unwanted areas.[43,50,58,59] To further tune the ink's thermophysical properties, ethylene glycol (EG) was added to the dispersion of the flakes in IPA in 1:1 (vol%) proportion. The addition of EG not only adjusts the ink fluidic properties, but also aids the circumvention of coffee-ring effect due to Marangoni flow in the droplet as mentioned previously. After the

preparation of the ink, SEM image of the flakes was taken to ensure the stability of the flakes in the solution and check for any possible agglomeration. No clusters of are observed As exhibited in Figure 5.3 (b). The concentration of the 1T-TaS_2 flakes in the ink was measured utilizing UV-visible spectroscopy (Agilent 60 UV/Vis). The ink was diluted 50 times and placed in a quartz cuvette (1 cm×1 cm) and the measurement was done in the wavelength range of 200 nm to 900 nm. An absorption peak is observed at ~280 nm related to the electron transition upon UV illumination.[163] The concentration of the flakes was determined using the Beer-Lambert law:[78,164] $A = \varepsilon C l$, in which A is the absorption, ε is the molar extinction coefficient ($M^{-1}cm^{-1}$), l is the length of light path (cm), and C is the concentration (M). The molar extinction coefficient of 1T-TaS_2 is 6×10^3 [Ref. [165]]. The concentration of flakes in the solution was calculated to be ~3.07 mg/mL. Based on the concentration and using the rule of mixtures, the density of the ink was calculated to be $\rho \sim 949.6$ (kg/m^3).

The surface tension of the ink was measured utilizing a CSC Scientific DuNouy interfacial tensiometer. This was done by inserting the device ring into the ink and raising the ring slowly until the film between the ink and the ring breaks. The surface tension of the ink was $\zeta \sim 2.94$ (N/m). For measuring the viscosity of the ink, a Cannon SimpleVIS viscometer was used. The measured kinematic viscosity displayed on the device was then divided by the density to calculate the dynamic viscosity as, $\mu \sim 5.85 \times 10^{-3}$ (Pa × s). Using a syringe with nozzle diameter of $210\ \mu m$, $Z \sim 13.1$ is obtained according to Equation (2-2). The obtained value is within the acceptable range which ensures a stable jetting and high print quality.

Figure 5.3 (c) shows a schematic of the printing procedure and the contacts in the printed device. Figure 5.3 (d), is a time-lapse optical image of the ink droplets falling down from the nozzle. As seen, no secondary or elongated droplets were formed during the printing process from because of perfectly tuned Z-number.

5.3 Printing of the Two-Terminal CDW device

To print the active channel for the two-terminal device used in this work, first sets are electrodes were fabricated on the substrate using e-beam lithography. Electrodes were made by e-beam evaporation of Ti and Au with the thickness of 10 nm and 100 nm, respectively. Then a lift-off method was used to remove excess metals from the surface. The CDW channel was printed on top of the electrodes afterwards. A blunt-end needle syringe with the nozzle diameter of 210 µm was used for dispensing of the ink. The temperature of the print bed was kept at 70 ℃ to expedite the drying of the ink and preventing the coffee-ring formation. 10 layers of material were printed on a Si/SiO_2 substrate. An optical image of the printed device is presented in Figure 5.3(e). The printed channel has the dimensions of 500 µm×3 µm×2 µm (L×W×t).

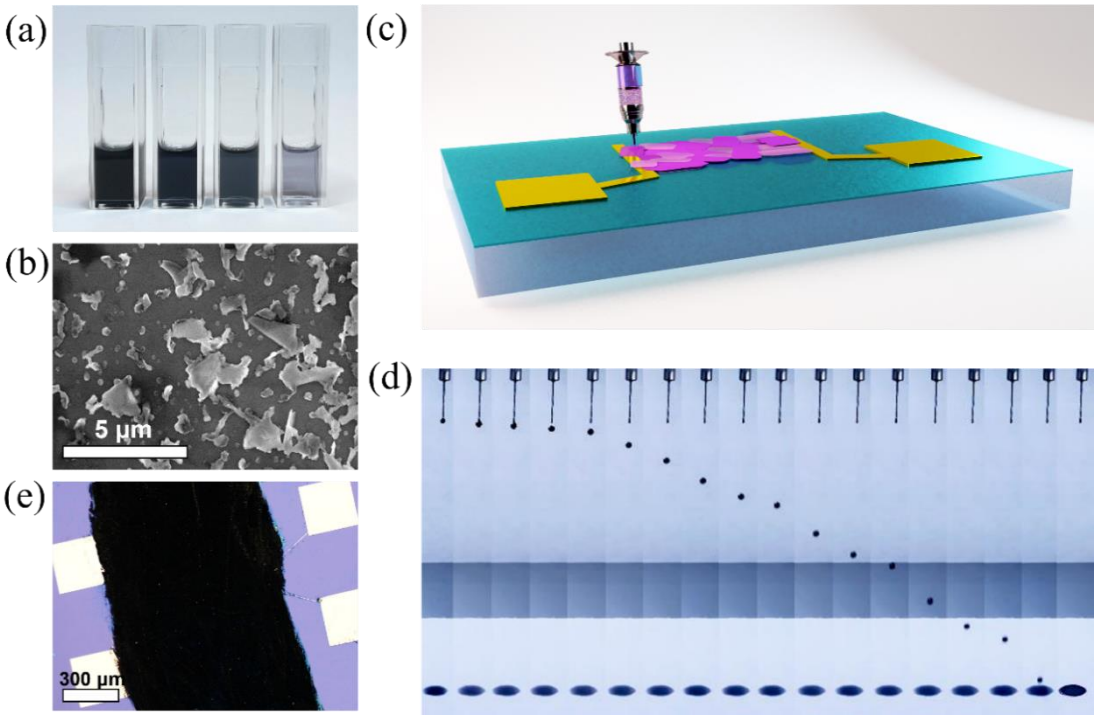

Figure 5.3. (a) Image of the exfoliated 1T-TaS_2 dispersed in isopropyl alcohol (IPA). The vial on the very left side includes the unsorted as-exfoliated 1T-TaS_2 flakes. Other three vials, from left to right, contain flakes with decreasing thicknesses; (b) SEM image of the exfoliated 1T-TaS_2 flakes in DMF, (c) schematic of the device printing process, (d) time-lapse optical image of the ink droplet formation and dispensing from the syringe needle to the substrate. No satellite or elongated droplets are formed, (e) optical microscopy image of the actual printed 1T-TaS_2 device.

5.4 Electrical Characterization and Low-Frequency Noise Measurements

The current–voltage (I–V) characteristics were measured in the cryogenic probe station (Lakeshore TTPX) with a semiconductor analyzer (Agilent B1500). The noise spectra were measured using a dynamic signal analyzer (Stanford Research 785). The bias voltage was supplied by a battery biasing circuit to minimize the noise at 60 Hz and the harmonics associated with it. The signal measured by the dynamic signal analyzer is the

absolute voltage noise spectral density, S_v, of a parallel resistance network consisting of a load resistor (R_L) of 3 KΩ and the device under test with a resistance of R_D. The normalized current noise spectral density, S_I/I^2, was calculated as $S_I/I^2 = S_V \times [(R_L + R_D)/(R_L \times R_D)]^2/(I^2 \times G)$ where G is the amplification of the low-noise amplifier.

5.5 Results and Discussion

5.5.1 I-V Characterization

The current-voltage characteristics of the printed devices were measured in the temperature range of 80 K to 400 K. The results are presented in Figure 5.4 (a). At high temperature ranges of $T > 340\,K$, the I-V curves are linear suggesting that the device exhibit ohmic contact characteristics. However, as the temperature decreases slight deviations from linearity in the I-V curves are observed. The latter is most likely due to the transition of the 1T-TaS_2 from IC-CDW to NC-CDW and then to C-CDW phases which accompanies with a small band-gap opening and thus, Schottky barrier formation at the contact interfaces. The resistance of the device at different temperatures for both heating and cooling cycles was extracted from the I-V curves and is shown in Figure 5.4 (b). The data reveal a hysteresis window at lower temperature range which is attributed to the C-CDW to NC-CDW phase transition. The formation of the hysteresis window is similar to the behavior of the two-terminal devices fabricated by mechanically exfoliated single crystal 1T-TaS_2. However, the NC-CDW to IC-CDW transition typically observed at

T~350 K in single-crystal devices is not observed in the printed devices. This might be due to the disordered nature of the printed devices.

The CDW transition in 1T-TaS_2 can be induced by stimuli other than the temperature variation.[29,64,140,151,166] For example, application of bias voltage may also trigger the CDW transition. However, it is still a point of debate whether the electric field directly sets off the transition or it is the Joule heating as a result of bias provokes the change. Figure 5.4 (c) and 5.4 (d) show the I-V characterization of the printed device under two different bias voltages. The experiments were carried out at $T = 110$ K below the C-CDW to NC-CDW since the change in the resistance is more prominent in this range. As one can see, as the bias increases to ~0.5 V, no transition is observed in the I-V curves (Figure 5 (c)). However, when the bias exceeds ~0.9 V, an abrupt jump in the current-voltage curve is observed. Nonetheless, it should be noted that, when bias is applied to the device, a full hysteresis loop similar to that observed in Figure 5 (b) is not observed. The latter suggest that the electric field might directly trigger the CDW transition as well.

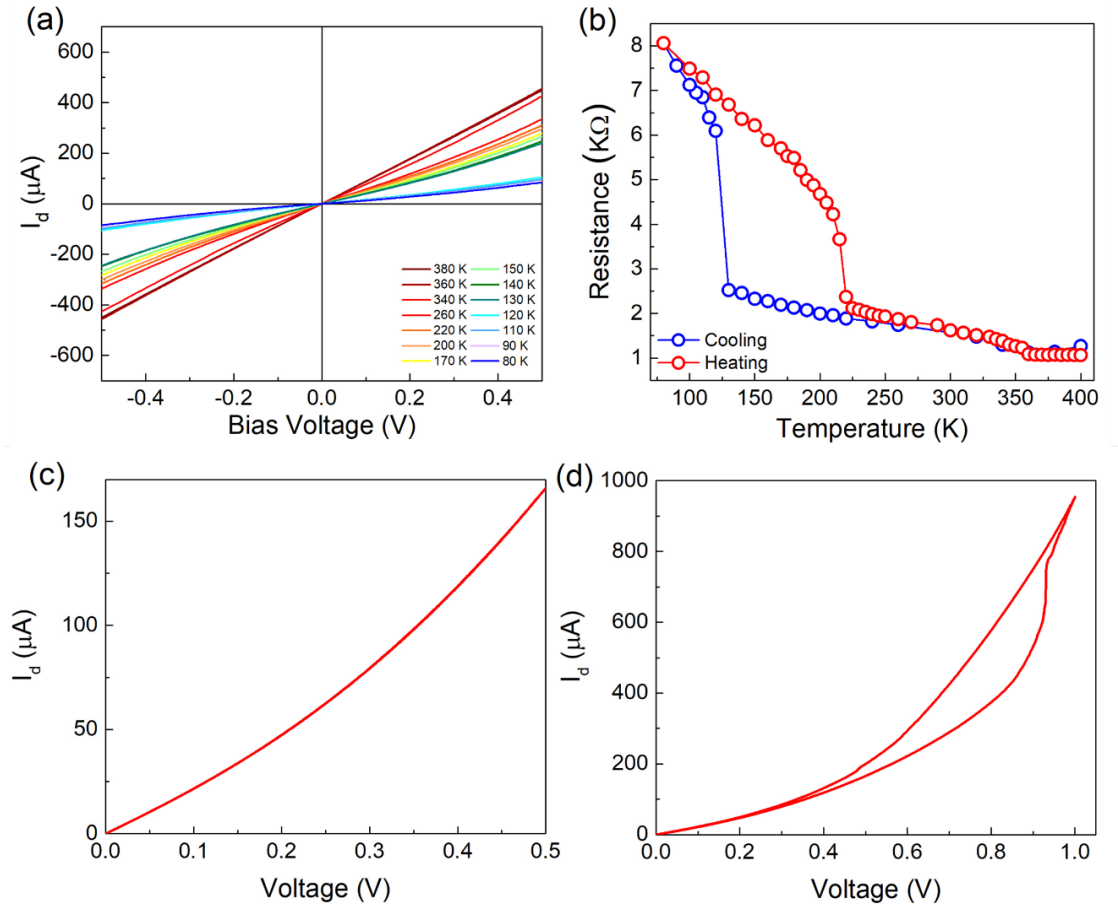

Figure 5.4. (a) Current-voltage curves of the printed device at different temperatures. The device has been cooled down from 380 K to 80 K. (b) Resistance of the 1T-TaS_2 device at different temperatures, (c) current-voltage characteristic of the device at 110 K. The bias voltage is swept from 0 up to 0.5 V, (d) current-voltage curve of the printed device at 110 K when the bias voltage is increased to 1 V.

5.5.2 Low-Frequency Noise Measurements

To further confirm the phase transition in the printed device, we used low-frequency noise spectroscopy.[29,61,62,138] The details of the experimental setup and measurement procedures have been reported elsewhere.[63,140] At the frequencies less than 100 kHz, materials often show the spectral noise density of $S(f) \sim 1/f^{\gamma}$ type, with $\gamma \sim 1$. Figure 5.5 (a) and 5.5 (b) shows the voltage-referred noise power spectral density, S_v, and the

normalized current noise power spectral density, S_I/I^2, as a function of frequency at different temperatures. In all experiments, the bias voltage was kept at ~0.1 V to avoid Joule heating. One can see that the noise spectrum follows the $1/f$ trend. Some traces of Lorentzian bulges at frequencies above *f*=100 Hz are observed that might be an indicative of defects or impurities.[142] Figure 5.5(c) and 5.5(d) exhibit noise power spectral density and normalized current noise power spectral density at the frequency of *f*=10 Hz as a function of temperature. Noise measurements were carried out when the device was cooled down from 400 K to 80 K with a cooling rate of 2 K/min. C-CDW to NC-CDW and NC-CDW to IC-CDW phase transitions are clearly observed as an abrupt increase in the noise spectral density. The temperatures at which the phase transitions happen agree with the finding from Figure 5.4. It is worth noting that the increase of noise spectral density is much sharper at lower temperature than the one for transition at higher temperatures (~340 K).

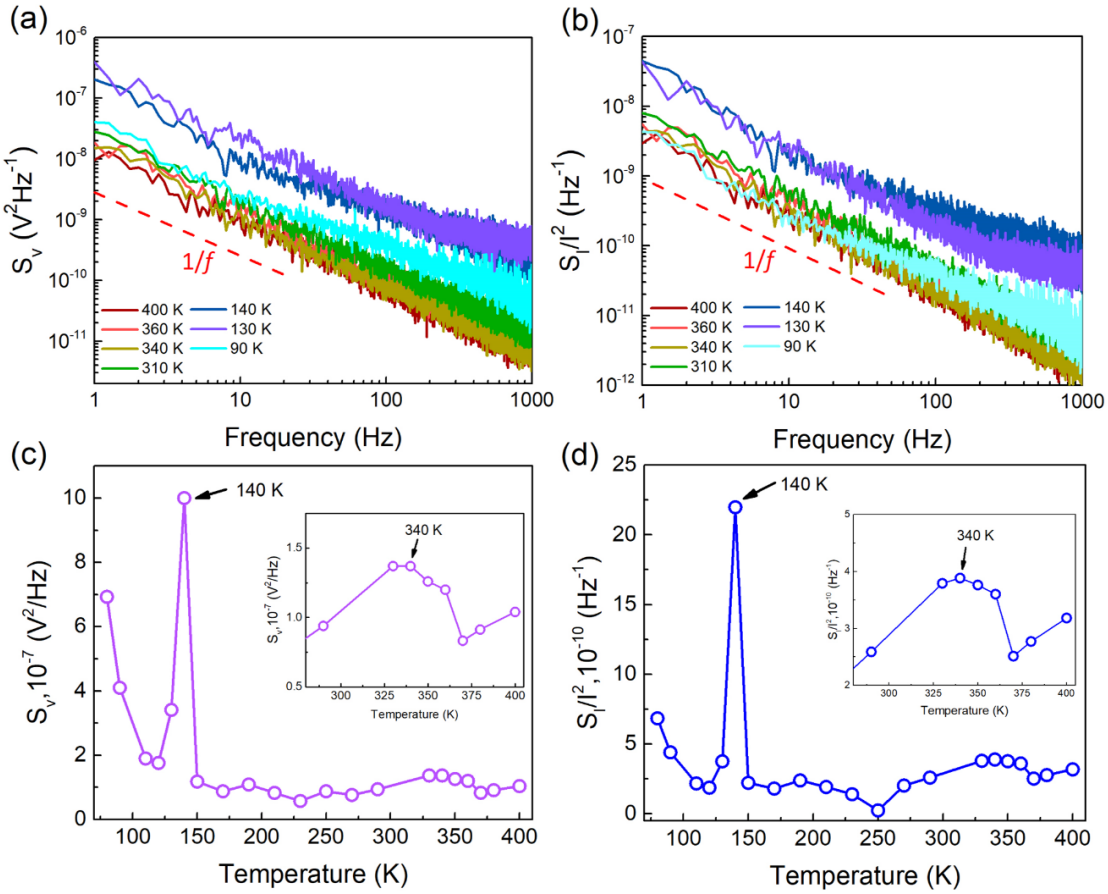

Figure 5.5. (a-b) S_v, and normalized noise data as a function of frequency at different temperatures. (c-d) S_v, and normalized noise data as a function of temperature at $f =$ 10 Hz when the device was cooled down from 400 K to 80 K. The device voltage was kept constant at 0.1 V.

5.6 Conclusions

In conclusion, we successfully printed two-terminal electronic devices based on 1T-TaS_2 CDW material. The crystals of TaS_2 were exfoliated by LPE technique in DMF. To prepare the ink, the solvent exchange was done, and the flakes were dispersed in a mixture of IPA and ethylene glycol. The results of I-V characterization and low-frequency electronic noise spectroscopy clearly confirmed the C-CDW to NC-CDW and NC-CDW

to IC-CDW states. We showed that by application of heat and bias voltage, the printed channel can undergo different CDW states. The findings can pave the way to fabricate novel printed electronic devices based on CDW layered vdW materials.

References

1. Wu, W. Inorganic Nanomaterials for Printed Electronics: A Review. *Nanoscale* **9**, 7342–7372 (2017).

2. McManus, D. *et al.* Water-Based and Biocompatible 2D Crystal Inks for All-Inkjet-Printed Heterostructures. *Nat. Nanotechnol.* **12**, 343–350 (2017).

3. Zschieschang, U. & Klauk, H. Organic Transistors on Paper: A Brief Review. *J. Mater. Chem. C* **7**, 5522–5533 (2019).

4. Kumar, R. *et al.* All-Printed, Stretchable Zn-Ag_2O Rechargeable Battery via Hyperelastic Binder for Self-Powering Wearable Electronics. *Adv. Energy Mater.* **7**, 1602096 (2017).

5. Karunakaran, S. K. *et al.* Recent Progress in Inkjet-Printed Solar Cells. *J. Mater. Chem. A* **7**, 13873–13902 (2019).

6. Eggenhuisen, T. M. *et al.* High Efficiency, Fully Inkjet Printed Organic Solar Cells with Freedom of Design. *J. Mater. Chem. A* **3**, 7255–7262 (2015).

7. Worsley, R. *et al.* All-2D Material Inkjet-Printed Capacitors: Toward Fully Printed Integrated Circuits. *ACS Nano* **13**, 54–60 (2019).

8. Lim, J. *et al.* All-Inkjet-Printed Metal-Insulator-Metal (MIM) Capacitor. *Curr. Appl. Phys.* **12**, e14–e17 (2012).

9. Moya, A., Gabriel, G., Villa, R. & Javier del Campo, F. Inkjet-Printed Electrochemical Sensors. *Curr. Opin. Electrochem.* **3**, 29–39 (2017).

10. Mani, N. K., Prabhu, A. & Kumar, A. S. Recent Updates on Inkjet-Printed Sensors. *Bioelectrochemical Interface Engineering* 371–384 (2019).

11. Tajima, R. *et al.* Truly Wearable Display Comprised of a Flexible Battery, Flexible Display Panel, and Flexible Printed Circuit. *J. Soc. Inf. Disp.* **22**, 237–244 (2014).

12. Conti, S., Lai, S., Cosseddu, P. & Bonfiglio, A. An Inkjet-Printed, Ultralow Voltage, Flexible Organic Field Effect Transistor. *Adv. Mater. Technol.* **2**, 1600212 (2017).

13. Dasgupta, S., Kruk, R., Mechau, N. & Hahn, H. Inkjet Printed, High Mobility Inorganic-Oxide Field Effect Transistors Processed at Room Temperature. *ACS Nano* **5**, 9628–9638 (2011).

14. Schaefer, D. & Cheung, W. M. Smart Packaging: Opportunities and Challenges.

Procedia CIRP **72**, 1022–1027 (2018).

15. Jeong, S. *et al.* Combined Role of Well-Dispersed Aqueous Ag Ink and the Molecular Adhesive Layer in Inkjet Printing the Narrow and Highly Conductive Ag Features on a Glass Substrate. *J. Phys. Chem. C* **114**, 22277–22283 (2010).

16. Kosmala, A., Wright, R., Zhang, Q. & Kirby, P. Synthesis of Silver Nano Particles and Fabrication of Aqueous Ag Inks for Inkjet Printing. *Mater. Chem. Phys.* **129**, 1075–1080 (2011).

17. Määttänen, A. *et al.* Inkjet-Printed Gold Electrodes on Paper: Characterization and Functionalization. *ACS Appl. Mater. Interfaces* **4**, 955–964 (2012).

18. Jeong, S. *et al.* Air-Stable, Surface-Oxide Free Cu Nanoparticles for Highly Conductive Cu Ink and Their Application to Printed Graphene Transistors. *J. Mater. Chem. C* **1**, 2704 (2013).

19. Capasso, A. *et al.* Ink-Jet Printing of Graphene for Flexible Electronics: An Environmentally-Friendly Approach. *Solid State Commun.* **224**, 53–63 (2015).

20. Song, J.-W. *et al.* Inkjet Printing of Single-Walled Carbon Nanotubes and Electrical Characterization of the Line Pattern. *Nanotechnology* **19**, 95702 (2008).

21. Rowley-Neale, S. J., Foster, C. W., Smith, G. C., Brownson, D. A. C. & Banks, C. E. Mass-Producible 2D-$MoSe_2$ Bulk Modified Screen-Printed Electrodes Provide Significant Electrocatalytic Performances Towards the Hydrogen Evolution Reaction. *Sustain. Energy Fuels* **1**, 74–83 (2017).

22. Li, J., Naiini, M. M., Vaziri, S., Lemme, M. C. & Östling, M. Inkjet Printing of MoS_2. *Adv. Funct. Mater.* **24**, 6524–6531 (2014).

23. Cho, B. *et al.* Chemical Sensing of 2D Graphene/MoS_2 Heterostructure Device. *ACS Appl. Mater. Interfaces* **7**, 16775–16780 (2015).

24. Kelly, A. G. *et al.* All-Printed Thin-Film Transistors from Networks of Liquid-Exfoliated Nanosheets. *Science* **356**, 69–73 (2017).

25. Madan, D. *et al.* Enhanced Performance of Dispenser Printed MA n-type Bi_2Te_3 Composite Thermoelectric Generators. *ACS Appl. Mater. Interfaces* **4**, 6117–6124 (2012).

26. Vaskivskyi, I. *et al.* Fast Electronic Resistance Switching Involving Hidden Charge Density Wave States. *Nat. Commun.* **7**, 11442 (2016).

27. Liu, G. *et al.* A Charge-Density-Wave Oscillator based on an Integrated Tantalum

Disulfide–Boron Nitride–Graphene Device Operating at Room Temperature. *Nat. Nanotechnol.* **11**, 845–850 (2016).

28. Liu, G. *et al.* Total-Ionizing-Dose Effects on Threshold Switching in 1T-TaS_2 Charge Density Wave Devices. *IEEE Electron Device Lett.* **38**, 1724–1727 (2017).

29. Geremew, A. K., Rumyantsev, S., Debnath, B., Lake, R. K. & Balandin, A. A. High-Frequency Current Oscillations in Charge-Density-Wave 1T-TaS_2 Devices: Revisiting the "Narrow Band Noise" Concept. *Appl. Phys. Lett.* **116**, 163101 (2020).

30. Khitun, A. G., Geremew, A. K. & Balandin, A. A. Transistor-Less Logic Circuits Implemented With 2-D Charge Density Wave Devices. *IEEE Electron Device Lett.* **39**, 1449–1452 (2018).

31. Molina-Mendoza, A. J. *et al.* High Current Density Electrical Breakdown of TiS_3 Nanoribbon-Based Field-Effect Transistors. *Adv. Funct. Mater.* **27**, 1605647 (2017).

32. Ghatak, S., Pal, A. N. & Ghosh, A. Nature of Electronic States in Atomically Thin MoS_2 Field-Effect Transistors. *ACS Nano* **5**, 7707–7712 (2011).

33. Wang, H. *et al.* Integrated Circuits Based on Bilayer MoS_2 Transistors. *Nano Lett.* **12**, 4674–4680 (2012).

34. Lipatov, A. *et al.* Few-Layered Titanium Trisulfide (TiS_3) Field-Effect Transistors. *Nanoscale* **7**, 12291–12296 (2015).

35. Riordan, M. The Lost History of the Transistor. *IEEE Spectr.* **41**, 44–49 (2003).

36. Zheng, Y., He, Z., Gao, Y. & Liu, J. Direct Desktop Printed-Circuits-on-Paper Flexible Electronics. *Sci. Reports 2013 31* **3**, 1–7 (2013).

37. Schackmar, F. *et al.* Perovskite Solar Cells with All-Inkjet-Printed Absorber and Charge Transport Layers. *Adv. Mater. Technol.* **6**, 2000271 (2021).

38. Fang, Y. *et al.* Inkjet-Printed Vertical Organic Field-Effect Transistor Arrays and Their Image Sensors. *ACS Appl. Mater. Interfaces* **10**, 30587–30595 (2018).

39. Park, J. *et al.* Research on Flexible Display at Ulsan National Institute of Science and Technology. *npj Flex. Electron. 2017 11* **1**, 1–13 (2017).

40. Schaefer, D. & Cheung, W. M. Smart Packaging: Opportunities and Challenges. *Procedia CIRP* **72**, 1022–1027 (2018).

41. Baraghani, S. *et al.* Printed Electronic Devices with Inks of TiS_3 Quasi-One-Dimensional van der Waals Material. *ACS Appl. Mater. Interfaces* **13**, 47033–47042 (2021).

42. Tomchenko, A. Printed Chemical Sensors: from Screen-Printing to Microprinting. in 279–290 (2006).

43. Hu, G. *et al.* Functional Inks and Printing of Two-Dimensional Materials. *Chem. Soc. Rev.* **47**, 3265–3300 (2018).

44. Bonaccorso, F., Bartolotta, A., Coleman, J. N. & Backes, C. 2D-Crystal-Based Functional Inks. *Adv. Mater.* **28**, 6136–6166 (2016).

45. Lilien, O. History of Industrial Gravure Printing up to 1920. *History of industrial gravure printing up to 1920* (1972).

46. Printing: Papermaking Science and Technology. (1998).

47. Leach, R. H., Pierce, R. J., Hickman, E. P., Mackenzie, M. J. & Smith, H. G. The Printing Ink Manual FIFTH EDITION Library of Congress Cataloging-in-Publication Data.

48. Zheng Cui, Chunshan Zhou, Song Qiu , Zheng Chen, Jian Lin , Jianwen Zhao , Changqi Ma, W. S. Printed Electronics: Materials, Techologies and Applications. 450 (2016).

49. Jun, H. Y., Lee, E. J. & Ryu, S. O. Synthesis and Characterization of Copper Ink and Direct Printing of Copper Patterns by Inkjet Printing for Electronic Devices. *Curr. Appl. Phys.* **20**, 853–861 (2020).

50. Torrisi, F. *et al.* Inkjet-Printed Graphene Electronics. *ACS Nano* **6**, 2992–3006 (2012).

51. Wang, C. *et al.* Advanced Carbon for Flexible and Wearable Electronics. *Adv. Mater.* **31**, 1801072 (2019).

52. Simon, J. & Langenscheidt, A. Curing Behavior of a UV-Curable Inkjet Ink: Distinction Between Surface-Cure and Deep-Cure Performance. *J. Appl. Polym. Sci.* **137**, 49218 (2020).

53. Chen, F. *et al.* Interface-Exfoliated Graphene-Based Conductive Screen-Printing Inks: Low-Loading, Low-Cost, and Additive-Free. *Sci. Rep.* **10**, 18047 (2020).

54. Zisman, W. A. Relation of the Equilibrium Contact Angle to Liquid and Solid Constitution. **16**, 5 (2021).

55. Deegan, R. D. *et al.* Capillary Flow as the Cause of Ring Stains from Dried Liquid Drops. *Nat. 1997 3896653* **389**, 827–829 (1997).

56. Larson, R. G. Transport and Deposition Patterns in Drying Sessile Droplets. *AIChE J.* **60**, 1538–1571 (2014).

57. Soft Matter. *Soft Matter* vol. 8 2686 (2012).

58. Jang, D., Kim, D. & Moon, J. Influence of Fluid Physical Properties on Ink-Jet Printability. *Langmuir* **25**, 2629–2635 (2009).

59. Derby, B. Inkjet Printing of Functional and Structural Materials: Fluid Property Requirements, Feature Stability, and Resolution. *Annu. Rev. Mater. Res.* **40**, 395–414 (2010).

60. Hu, G. *et al.* Black Phosphorus Ink Formulation for Inkjet Printing of Optoelectronics and Photonics. *Nat. Commun.* **8**, 278 (2017).

61. Salgado, R. *et al.* Low-Frequency Noise Spectroscopy of Charge-Density-Wave Phase Transitions in Vertical Quasi-2D 1T-TaS_2 Devices. *Appl. Phys. Express* **12**, 037001 (2019).

62. Ghosh, S., Kargar, F., Mohammadzadeh, A., Rumyantsev, S. & Balandin, A. A. Low-Frequency Electronic Noise Spectroscopy of Quasi-2D van der Waals Antiferromagnetic Semiconductors. (2021).

63. Mohammadzadeh, A. *et al.* Room Temperature Depinning of the Charge-Density Waves in Quasi-Two-Dimensional 1T-TaS_2 Devices. *Appl. Phys. Lett.* **118**, 223101 (2021).

64. Mohammadzadeh, A. *et al.* Evidence for a Thermally Driven Charge-Density-Wave Transition in 1T-TaS_2 Thin-Film Devices: Prospects for GHz Switching Speed. *Appl. Phys. Lett.* **118**, 093102 (2021).

65. Desai, S. B. *et al.* Gold-Mediated Exfoliation of Ultralarge Optoelectronically-Perfect Monolayers. *Adv. Mater.* **28**, 4053–4058 (2016).

66. Pető, J. *et al.* Spontaneous Doping of the Basal Plane of MoS_2 Single Layers Through Oxygen Substitution Under Ambient Conditions. *Nat. Chem.* **10**, 1246–1251 (2018).

67. Radisavljevic, B., Radenovic, A., Brivio, J., Giacometti, V. & Kis, A. Single-Layer MoS_2 Transistors. *Nat. Nanotechnol.* **6**, 147–150 (2011).

68. McCreary, A. *et al.* Intricate Resonant Raman Response in Anisotropic ReS_2. *Nano Lett.* **17**, 5897–5907 (2017).

69. Gao, X., Bian, G. & Zhu, J. Electronics from Solution-Processed 2D Semiconductors. *J. Mater. Chem. C* **7**, 12835–12861 (2019).

70. Kang, J., Sangwan, V. K., Wood, J. D. & Hersam, M. C. Solution-Based Processing of Monodisperse Two-Dimensional Nanomaterials. *Acc. Chem. Res.* **50**, 943–951 (2017).

71. Backes, C. *et al.* Guidelines for Exfoliation, Characterization and Processing of Layered Materials Produced by Liquid Exfoliation. *Chemistry of Materials* vol. 29 243–255 (2017).

72. Barani, Z. *et al.* Electrically Insulating Flexible Films with Quasi-1D van der Waals Fillers as Efficient Electromagnetic Shields in the GHz and Sub-THz Frequency Bands. *Adv. Mater.* **33**, 2007286 (2021).

73. Nicolosi, V., Chhowalla, M., Kanatzidis, M. G., Strano, M. S. & Coleman, J. N. Liquid Exfoliation of Layered Materials. *Science* vol. 340 (2013).

74. McCord, M. a & Rooks, M. J. SPIE Handbook of Micromachining and Microfabrication Volume 1. *SPIE Handb. Microlithogr. Micromach. Microfabr.* **1**, (2000).

75. Tseng, A. A., Chen, K., Chen, C. D. & Ma, K. J. Electron Beam Lithography in Nanoscale Fabrication: Recent Development. *IEEE Trans. Electron. Packag. Manuf.* **26**, 141–149 (2003).

76. Hu, G. *et al.* A General Ink Formulation of 2D Crystals for Wafer-Scale Inkjet Printing. *Sci. Adv.* **6**, eaba5029 (2020).

77. Bidoki, S. *et al.* Inkjet Printing of Conductive Patterns on Textile Fabrics. *AATCC Rev.* **5**, 11–14 (2005).

78. Carey, T. *et al.* Fully Inkjet-Printed Two-Dimensional Material Field-Effect Heterojunctions for Wearable and Textile Electronics. *Nat. Commun.* **8**, 1202 (2017).

79. Redinger, D., Molesa, S., Yin, S., Farschi, R. & Subramanian, V. An Ink-Jet-Deposited Passive Component Process for RFID. *IEEE Trans. Electron Devices*

51, 1978–1983 (2004).

80. Park, S.-I. *et al.* Printed Assemblies of Inorganic Light-Emitting Diodes for Deformable and Semitransparent Displays. *Science* **325**, 977 LP – 981 (2009).

81. Ganesan, S., Mehta, S. & Gupta, D. Fully Printed Organic Solar Cells – A Review of Techniques, Challenges and Their Solutions. *Opto-Electronics Rev.* **27**, 298–320 (2019).

82. Tortorich, R. P. & Choi, J.-W. Inkjet Printing of Carbon Nanotubes. *Nanomater.* **3**, 453–468 (2013).

83. Akinwande, D., Petrone, N. & Hone, J. Two-Dimensional Flexible Nanoelectronics. *Nat. Commun.* **5**, 5678 (2014).

84. Franklin, A. D. Nanomaterials in Transistors: From High-Performance to Thin-Film Applications. *Science* **349**, aab2750 (2015).

85. Chhowalla, M. *et al.* The Chemistry of Two-Dimensional Layered Transition Metal Dichalcogenide Nanosheets. *Nat. Chem.* **5**, 263–275 (2013).

86. Jariwala, D., Sangwan, V. K., Lauhon, L. J., Marks, T. J. & Hersam, M. C. Emerging Device Applications for Semiconducting Two-Dimensional Transition Metal Dichalcogenides. *ACS Nano* **8**, 1102–1120 (2014).

87. Wang, Q. H., Kalantar-Zadeh, K., Kis, A., Coleman, J. N. & Strano, M. S. Electronics and Optoelectronics of Two-Dimensional Transition Metal Dichalcogenides. *Nat. Nanotechnol.* **7**, 699–712 (2012).

88. Island, J. O. *et al.* Electronics and Optoelectronics of Quasi-1D Layered Transition Metal Trichalcogenides. *2D Mater.* **4**, 22003 (2017).

89. Randle, M. D. *et al.* Collective States and Charge Density Waves in the Group IV Transition Metal Trichalcogenides. *Appl. Phys. Lett.* **118**, 210502 (2021).

90. Stolyarov, M. A. *et al.* Breakdown Current Density in h-BN-Capped Quasi-1D $TaSe_3$ Metallic Nanowires: Prospects of Interconnect Applications. *Nanoscale* **8**, 15774–15782 (2016).

91. Abdulsalam, M. & Joubert, D. P. Structural and Electronic Properties of MX_3 (M = Ti, Zr and Hf; X = S, Se, Te) from First Principles Calculations. *Eur. Phys. J. B* **88**, 177 (2015).

92. Island, J. O. *et al.* Titanium trisulfide (TiS_3): A 2D Semiconductor with Quasi-1D

Optical and Electronic Properties. *Sci. Rep.* **6**, 22214 (2016).

93. Lipatov, A. *et al.* Quasi-1D TiS_3 Nanoribbons: Mechanical Exfoliation and Thickness-Dependent Raman Spectroscopy. *ACS Nano* **12**, 12713–12720 (2018).

94. Muratov, D. S. *et al.* Synthesis and Exfoliation of Quasi-1D $(Zr,Ti)S_3$ Solid Solutions for Device Measurements. *J. Alloys Compd.* **815**, 152316 (2020).

95. Gilbert, S. J. *et al.* Effect of Band Symmetry on Photocurrent Production in Quasi-One-Dimensional Transition-Metal Trichalcogenides. *ACS Appl. Mater. Interfaces* **12**, 40525–40531 (2020).

96. Zybtsev, S. G. *et al.* NbS_3: A Unique Quasi-One-Dimensional Conductor with Three Charge Density Wave Transitions. *Phys. Rev. B* **95**, 35110 (2017).

97. Pant, A. *et al.* Strong Dichroic Emission in the Pseudo One Dimensional Material ZrS_3. *Nanoscale* **8**, 16259–16265 (2016).

98. Muratov, D. S. *et al.* Slot-Die-Printed Two-Dimensional ZrS_3 Charge Transport Layer for Perovskite Light-Emitting Diodes. *ACS Appl. Mater. Interfaces* **11**, 48021–48028 (2019).

99. Geremew, A. *et al.* Current Carrying Capacity of Quasi-1D $ZrTe_3$ Van Der Waals Nanoribbons. *IEEE Electron Device Lett.* **39**, 735–738 (2018).

100. Island, J. O. *et al.* Ultrahigh Photoresponse of Few-Layer TiS_3 Nanoribbon Transistors. *Adv. Opt. Mater.* **2**, 641–645 (2014).

101. Bigg, D. M. & Stutz, D. E. Plastic Composites for Electromagnetic Interference Shielding Applications. *Polym. Compos.* **4**, 40–46 (1983).

102. Pan, Y. *et al.* Percolation Threshold and Electrical Conductivity of a Two-Phase Composite Containing Randomly Oriented Ellipsoidal Inclusions. *J. Appl. Phys.* **110**, 123715 (2011).

103. Murphy, D. W. & Trumbore, F. A. The Chemistry of TiS_3 and $NbSe_3$ Cathodes. *J. Electrochem. Soc.* **123**, 960–964 (1976).

104. Kikkawa, S., Koizumi, M., Yamanaka, S., Onuki, Y. & Tanuma, S. Electrical Conductivity of TiS_3. *Phys. status solidi* **61**, K55–K57 (1980).

105. Hsieh, P.-L., Jackson, C. M. & Grüner, G. Disorder Effects in the Linear Chain Compound TiS_3. *Solid State Commun.* **46**, 505–507 (1983).

106. Gorochov, O., Katty, A., Le Nagard, N., Levy-Clement, C. & Schleich, D. M. Photoelectrochemical Study of TiS_3 in Aqueous Solution. *Mater. Res. Bull.* **18**, 111–118 (1983).

107. Finkman, E. & Fisher, B. Electrical Transport Measurements in TiS_3. *Solid State Commun.* **50**, 25–28 (1984).

108. Gorlova, I. G., Pokrovskii, V. Y., Zybtsev, S. G., Titov, A. N. & Timofeev, V. N. Features of the Conductivity of the Quasi-One-Dimensional Compound TiS_3. *J. Exp. Theor. Phys.* **111**, 298–303 (2010).

109. Gorlova, I. G. *et al.* Nonlinear Conductivity of Quasi-One-Dimensional Layered Compound TiS_3. *Phys. B Condens. Matter* **407**, 1707–1710 (2012).

110. Ferrer, I. J., Maciá, M. D., Carcelén, V., Ares, J. R. & Sánchez, C. On the Photoelectrochemical Properties of TiS_3 Films. *Energy Procedia* **22**, 48–52 (2012).

111. Ferrer, I. J., Ares, J. R., Clamagirand, J. M., Barawi, M. & Sánchez, C. Optical Properties of Titanium Trisulphide (TiS_3) Thin Films. *Thin Solid Films* **535**, 398–401 (2013).

112. Yi, H. *et al.* The Band Structure of the Quasi-One-Dimensional Layered Semiconductor TiS_3(001). *Appl. Phys. Lett.* **112**, 52102 (2018).

113. Randle, M. *et al.* Gate-Controlled Metal–Insulator Transition in TiS_3 Nanowire Field-Effect Transistors. *ACS Nano* **13**, 803–811 (2019).

114. Cui, Q. *et al.* Time-Resolved Measurements of Photocarrier Dynamics in TiS_3 Nanoribbons. *ACS Appl. Mater. Interfaces* **8**, 18334–18338 (2016).

115. Dai, J. & Zeng, X. C. Titanium Trisulfide Monolayer: Theoretical Prediction of a New Direct-Gap Semiconductor with High and Anisotropic Carrier Mobility. *Angew. Chemie Int. Ed.* **54**, 7572–7576 (2015).

116. Dhingra, A., Lipatov, A., Loes, M. J., Sinitskii, A. & Dowben, P. A. Nonuniform Debye Temperatures in Quasi-One-Dimensional Transition-Metal Trichalcogenides. *ACS Mater. Lett.* **3**, 414–419 (2021).

117. Gorlova, I. G. & Pokrovskii, V. Y. Collective Conduction Mechanism in a Quasi-One-Dimensional TiS_3 Compound. *JETP Lett.* **90**, 295–298 (2009).

118. Frisenda, R. *et al.* Dielectrophoretic Assembly of Liquid-Phase-Exfoliated TiS_3 Nanoribbons for Photodetecting Applications. *Chem. Commun.* **53**, 6164–6167 (2017).

119. Furuseth, S., Brattås, L., Kjekshus, A., Andresen, A. & Fischer, P. On the Crystal Structures of TiS_3, ZrS_3, $ZrSe_3$, $ZrTe_3$, HfS_3, and $HfSe_3$. *Acta Chem. Scand.* 623–631 (1975).

120. Nečas, D. & Klapetek, P. Gwyddion: An Open-Source Software for SPM Data Analysis. *Open Phys.* **10**, 181–188 (2012).

121. Wu, K. *et al.* Unusual Lattice Vibration Characteristics in Whiskers of the Pseudo-One-Dimensional Titanium Trisulfide TiS_3. *Nat. Commun.* **7**, 12952 (2016).

122. Galliardt, D. W., Nieveen, W. R. & Kirby, R. D. Lattice Properties of the Linear Chain Compound TiS_3. *Solid State Commun.* **34**, 37–39 (1980).

123. Gard, P., Cruege, F., Sourisseau, C. & Gorochov, O. Single-Crystal Micro-Raman Studies of ZrS_3, TiS_3 and Several $Zr_{1-x}Ti_xS_3$ compounds ($0<x\leqslant 0.33$). *J. Raman Spectrosc.* **17**, 283–288 (1986).

124. Soltman, D. & Subramanian, V. Inkjet-Printed Line Morphologies and Temperature Control of the Coffee Ring Effect. *Langmuir* **24**, 2224–2231 (2008).

125. Fromm, J. E. Numerical Calculation of the Fluid Dynamics of Drop-on-Demand Jets. *IBM J. Res. Dev.* **28**, 322–333 (1984).

126. Shin, P., Sung, J. & Lee, M. H. Control of Droplet Formation for Low Viscosity Fluid by Double Waveforms Applied to a Piezoelectric Inkjet Nozzle. *Microelectron. Reliab.* **51**, 797–804 (2011).

127. Dong, H., Carr, W. W. & Morris, J. F. An Experimental Study of Drop-On-Demand Drop Formation. *Phys. Fluids* **18**, 72102 (2006).

128. de Gans, B.-J., Kazancioglu, E., Meyer, W. & Schubert, U. S. Ink-jet Printing Polymers and Polymer Libraries Using Micropipettes. *Macromol. Rapid Commun.* **25**, 292–296 (2004).

129. Gilbert, S. J. *et al.* The Electronic Properties of Au and Pt Metal Contacts on Quasi-One-Dimensional Layered TiS_3(001). *Appl. Phys. Lett.* **114**, 101604 (2019).

130. Baranovskii, S. & Rubel, O. Charge Transport in Disordered Materials. in *Springer Handbook of Electronic and Photonic Materials* (eds. Kasap, S. & Capper, P.) 1 (Springer International Publishing, 2017).

131. Zubair Ansari, M. & Khare, N. Thermally Activated Band Conduction and Variable Range Hopping Conduction in Cu_2ZnSnS_4 Thin Films. *J. Appl. Phys.*

117, 25706 (2015).

132. Chiu, F.-C. A Review on Conduction Mechanisms in Dielectric Films. *Adv. Mater. Sci. Eng.* **2014**, 578168 (2014).

133. Mott, N. F. Conduction in Glasses Containing Transition Metal Ions. *J. Non. Cryst. Solids* **1**, 1–17 (1968).

134. Efros, A. L. & Shklovskii, B. I. Coulomb Gap and Low Temperature Conductivity of Disordered Systems. *J. Phys. C Solid State Phys.* **8**, L49–L51 (1975).

135. Kumar, R. & Khare, N. Temperature Dependence of Conduction Mechanism of ZnO and Co-Doped ZnO Thin Films. *Thin Solid Films* **516**, 1302–1307 (2008).

136. Prudenziati, M., Hormadaly, J. & Prudenziati, M. *Printed Films : Materials Science and Applications in Sensors, Electronics and Photonics*. (2012).

137. Wang, F. *et al.* Inter-Flake Quantum Transport of Electrons and Holes in Inkjet-Printed Graphene Devices. *Adv. Funct. Mater.* **31**, 2007478 (2021).

138. Geremew, A. *et al.* Low-Frequency Electronic Noise in Superlattice and Random-Packed Thin Films of Colloidal Quantum Dots. *Nanoscale* **11**, 20171–20178 (2019).

139. Guyot-Sionnest, P. Electrical Transport in Colloidal Quantum Dot Films. *J. Phys. Chem. Lett.* **3**, 1169–1175 (2012).

140. Salgado, R. *et al.* Low-Frequency Noise Spectroscopy of Charge-Density-Wave Phase Transitions in Vertical Quasi-2D 1T-TaS_2 Devices. *Appl. Phys. Express* **12**, 037001 (2019).

141. Liu, G., Rumyantsev, S., Bloodgood, M. A., Salguero, T. T. & Balandin, A. A. Low-Frequency Current Fluctuations and Sliding of the Charge Density Waves in Two-Dimensional Materials. *Nano Lett.* **18**, 3630–3636 (2018).

142. Balandin, A. A. *Noise and fluctuations control in electronic devices*. (American Scientific Publishers, 2002).

143. Jakus, A. E. *et al.* Three-Dimensional Printing of High-Content Graphene Scaffolds for Electronic and Biomedical Applications. *ACS Nano* **9**, 4636–4648 (2015).

144. Kim, J., Kumar, R., Bandodkar, A. J. & Wang, J. Advanced Materials for Printed Wearable Electrochemical Devices: A Review. *Adv. Electron. Mater.* **3**, 1600260

(2017).

145. Nag, A., Mukhopadhyay, S. C. & Kosel, J. Wearable Flexible Sensors: A Review. *IEEE Sens. J.* **17**, 3949–3960 (2017).

146. Abellán-Llobregat, A. *et al.* A Stretchable and Screen-Printed Electrochemical Sensor for Glucose Determination in Human Perspiration. *Biosens. Bioelectron.* **91**, 885–891 (2017).

147. Mannoor, M. S. *et al.* Graphene-Based Wireless Bacteria Detection on Tooth Enamel. *Nat. Commun.* **3**, 763 (2012).

148. Fan, Z., Wei, T., Luo, G. & Wei, F. Fabrication and Characterization of Multi-Walled Carbon Nanotubes-Based Ink. *J. Mater. Sci.* **40**, 5075–5077 (2005).

149. Liu, G. *et al.* A Charge-Density-Wave Oscillator Based on an Integrated Tantalum Disulfide–Boron Nitride–Graphene Device Operating at Room Temperature. *Nat. Nanotechnol.* **11**, 845–850 (2016).

150. Wen, W. *et al.* Light-Tunable 1T-TaS_2 Charge-Density-Wave Oscillators. *Nano Lett.* **12**, 37001 (2015).

151. Geremew, A. K. *et al.* Bias-Voltage Driven Switching of the Charge-Density-Wave and Normal Metallic Phases in 1T-TaS_2 Thin-Film Devices. *ACS Nano* **13**, 7231–7240 (2019).

152. Sipos, B. *et al.* From Mott State to Superconductivity in 1T-TaS_2. *Nat. Mater.* **7**, 960–965 (2008).

153. Börner, P. C. *et al.* Observation of Charge Density Waves in Free-Standing 1T-$TaSe_2$ Monolayers by Transmission Electron Microscopy. *Appl. Phys. Lett.* **113**, 173103 (2018).

154. Samnakay, R. *et al.* Zone-Folded Phonons and the Commensurate-Incommensurate Charge-Density-Wave Transition in 1T -$TaSe_2$ Thin Films. *Nano Lett.* **15**, 2965–2973 (2015).

155. Renteria, J. *et al.* All-Metallic Electrically Gated 2H-$TaSe_2$ Thin-Film Switches and Logic Circuits. *J. Appl. Phys.* **115**, 34305 (2014).

156. Sugai, S., Murase, K., Uchida, S. & Tanaka, S. Comparison of the Soft Modes in Tantalum Dichalcogenides. *Phys. B-condensed Matter* **105**, 405–409 (1981).

157. Hirata, T. & Ohuchi, F. Temperature Dependence of the Raman Spectra of 1T-

TaS_2. *Solid State Commun.* **117**, 361–364 (2001).

158. He, R. *et al.* Distinct Surface and Bulk Charge Density Waves in Ultrathin 1T−TaS_2. *Phys. Rev. B* **94**, 201108 (2016).

159. Duffey, J. R., Kirby, R. D. & Coleman, R. V. Raman Scattering from 1T-TaS_2. *Solid State Commun.* **20**, 617–621 (1976).

160. Zhao, R. *et al.* Two-Dimensional Tantalum Disulfide: Controlling Structure and Properties via Synthesis. *2D Mater.* **5**, 025001 (2018).

161. Albertini, O. R. *et al.* Zone-Center Phonons of Bulk, Few-Layer, and Monolayer 1T−TaS_2 : Detection of Commensurate Charge Density Wave Phase Through Raman Scattering. *Phys. Rev. B* **93**, 214109 (2016).

162. Zhao, R. *et al.* Tuning Phase Transitions in 1T-TaS_2 via the Substrate. *Nano Lett.* **17**, 3471–3477 (2017).

163. Zhou, L. *et al.* Tantalum Disulfide Quantum Dots: Preparation, Structure, and Properties. *Nanoscale Res. Lett.* **15**, 20 (2020).

164. Lotya, M. *et al.* Liquid Phase Production of Graphene by Exfoliation of Graphite in Surfactant/Water Solutions. *J. Am. Chem. Soc.* **131**, 3611–3620 (2009).

165. Murphy, D. W. & Hull, G. W. Monodispersed Tantalum Disulfide and Adsorption Complexes with Cations. *J. Chem. Phys.* **62**, 973–978 (1975).

166. Tsen, A. W. *et al.* Structure and Control of Charge Density Waves in Two-Dimensional 1T-TaS_2. *Proc. Natl. Acad. Sci.* **112**, 15054–15059 (2015).